CrossMark

Physical Environments of the Luminosity Outburst Source NGC 6334I Traced by Thermal and Maser Lines of Multiple Molecules

Jiong-Heng Wu[1], Xi Chen[1,2] , Yan-Kun Zhang[1] , Simon P. Ellingsen[3] , Andrej M. Sobolev[4], Zhang Zhao[2], Shi-Ming Song[2] ,
Zhi-Qiang Shen[2] , Bin Li[2], Bo Xia[2], Rong-Bin Zhao[2], Jing-Qing Wang[2], and Ya-Jun Wu[2]

[1] Center for Astrophysics, Guangzhou University, Guangzhou 510006, People's Republic of China; chenxi@gzhu.edu.cn
[2] Shanghai Astronomical Observatory, Chinese Academy of Sciences, 80 Nandan Road, Shanghai 200030, People's Republic of China
[3] School of Natural Sciences, University of Tasmania, Private Bag 37, Hobart, Tasmania 7001, Australia
[4] Ural Federal University, 19 Mira Street, 620002 Ekaterinburg, Russia

Abstract

We have conducted a systematic line survey, primarily focused on transitions of the methanol and ammonia molecules, and monitoring observations of masers toward the high-mass star-forming region NGC 6334I. These observations were undertaken between 2019 and 2022 in the *C, K, Ka*, and *Q* bands with the Tianma Radio Telescope. In total, 63 CH_3OH (including 11 class I and nine class II maser or maser candidate), 18 $^{13}CH_3OH$, and 34 NH_3 (including seven maser or maser candidate) transitions were detected. The emission is likely associated with the luminosity outburst source MM1. Rotation diagram analysis of multiple ammonia transitions shows that the gas temperature in the molecular core was a factor of 2 higher than that measured in previous observations in the pre-burst stage. This suggests that the molecular core has likely been heated by radiation originating from the luminosity outburst. Maser variability in the methanol and excited-state OH masers shows a general trend that the maser components associated with the luminosity outburst have decreased in their intensity since 2020. The decay in the maser luminosity indicates that the outburst is possibly declining, and as a result, the duration of the MM1 luminosity outburst may be shorter than the predicted 40 yr duration. Compared to the masers detected toward another luminosity outburst source, G358.93-0.03, abundant class I methanol masers and strong water maser flares were also detected toward NGC 633I, but masers from rare class II methanol transitions and new molecules were absent toward NGC 6334I. The large number of detections of maser transitions toward the two burst sources provided a database for further maser modeling to explore the physical environments associated with accretion burst events.

Unified Astronomy Thesaurus concepts: Interstellar masers (846); Star formation (1569); Accretion (14); Massive stars (732); Young stellar objects (1834)

1. Introduction

Young stellar objects (YSOs) are increasingly assumed to be susceptible to accretion burst phenomena mediated by disks (Kenyon et al. 1990; Evans et al. 2009). During bursts, YSOs are detected with luminosity outbursts due to accretion rate increments (Offner & McKee 2011). For low-mass YSOs, luminosity outbursts have been detected with variations of 5 or more magnitudes in the FU Orionis stars (Herbig 1989), and 2–3 mag in the EX Lupi stars (Herbig 1977). Outbursts of these objects can occur over a period of weeks to decades (Audard et al. 2014). In recent years, studies of Orion molecular clouds have shown that episodic accretion accounts for ⩾25% of the mass of low-mass stars (Fischer et al. 2019). Recent theoretical and observational studies have revealed that episodic accretion and outburst phenomena can also occur in high-mass YSOs (HMYSOs; e.g., Meyer et al. 2017, 2019), similar to those occurring in low-mass star formation. Luminosity outbursts have been detected in several HMYSOs in the infrared and millimeter bands, for example, S255IR-NIRS3 (Carattio Garatti et al. 2017), NGC 6334I-MM1 (Hunter et al. 2017, 2021), and G358.93-0.03 (Stecklum et al. 2021). Compared to low-mass stars, high-mass stars can even gain 40%–60% of their mass during accretion bursts based on theoretical considerations (Meyer et al. 2021), suggesting that it is an essential process for high-mass star formations (Brogan et al. 2018; Cesaroni et al. 2018).

The study of episodic accretion bursts in HMYSOs is crucial for enhancing our understanding of whether episodic accretion is a common phenomenon in the formation of young stars. However, compared with low-mass YSOs, the deeply embedded nature of accreting HMYSOs impedes observations and hampers the direct investigation of their accretion processes. Fortunately, masers can be effective tracers of several transient YSO events because they are thought to detect changes in the physical conditions of their natal clouds caused by radiation field enhancement and matter collision. In particular, class II CH_3OH (methanol) masers are pumped by infrared radiation and are thought to be closely associated with HMYSO luminosity outbursts. It is worth mentioning that a direct link between the 6.7 GHz class II CH_3OH maser flaring and accretion burst has recently been established only in a small number of HMYSOs, e.g., G358.93-0.03-MM1 (Breen et al. 2019; MacLeod et al. 2019; Sugiyama et al. 2019; Burns et al. 2020), S255IR-NIRS3 (Fujisawa et al. 2015; Carattio Garatti et al. 2017; Moscadelli et al. 2017), and NGC 6334I-MM1 (Hunter et al. 2017, 2018; MacLeod et al. 2018). Besides, 22 GHz H_2O (water) maser emission from protostars has exhibited flare phenomena toward Orion KL (Abraham et al. 1981; Omodaka et al. 1999; Hirota et al. 2014), W49N

(Liljeström & Gwinn 2000; Honma et al. 2004), G25.65 + 1.05 (Volvach et al. 2017a, 2017b; Lekht et al. 2018), G358.93-0.03 (Bayandina et al. 2022; Miao et al. 2022), and W51D (Zhang et al. 2022).

During the accretion burst stage, new maser species may be energized in exotic or rare physical conditions induced by accretion bursts, corresponding to the best epoch to search for and identify new maser species. More than 30 new methanol maser transitions have been detected toward a short-lived (within a few months) accretion burst source G358.93-0.03 (Breen et al. 2019; Brogan et al. 2019; MacLeod et al. 2019; Miao et al. 2022), and some masers from new species (such as CH_3OH, HDO, and HNCO) have also been detected toward this source (Chen et al. 2020a, 2020b). The latter three new species of masers provide solid contributions to the episodic accretion scheme because they accurately trace spiral-arm accretion flow structures caused by the gravitational instability of large-mass disks (Chen et al. 2020b). It should be noted that all of the newly detected methanol masers toward this source belong to class II transitions, supporting the idea that these new maser transitions are pumped by the increased local radiation field due to the stellar luminosity burst. The discovery of these new maser transitions further suggests that the episodic accretion process can induce special physical environments to effectively produce new and rare masers from methanol and other molecular species. However, the search for new maser transitions toward additional accretion burst sources is still required to confirm the universality of the special environments associated with accretion bursts.

Drastic changes in the temperature and density in high-mass star-forming regions (HMSFRs) might be triggered by an accretion burst. In particular, heat-wave propagation is thought to be involved in episodic accretion (Burns et al. 2020), resulting in inside-out heating of the molecular core wherein high-mass stars are formed. Identifying additional tracers for these drastic events will help us explore episodic accretion burst events. Ammonia (NH_3), which is called the "interstellar thermometer," is known to be a very useful tool for diagnosing the variations of gas temperatures in HMSFRs. Therefore, the transitions from this molecule can be used to trace the heat-wave propagation process. An attempt was made to detect possible heat-wave propagation toward accretion burst candidate W51D (Zhang et al. 2022). Abundant NH3 maser transitions have also been detected toward accretion burst candidates W51D (Zhang et al. 2022) and G358.93-0.03 (McCarthy et al. 2023). Therefore, both thermal and maser emissions from ammonia may be used to investigate the variability in accretion bursts.

The target source of this study, NGC 6334I is a well-known source of accretion bursts identified from luminosity outbursts in multiwavelength observations since mid-2015, including mid-infrared (Hunter et al. 2021), millimeter (Hunter et al. 2017), and radio masers (Hunter et al. 2018; MacLeod et al. 2018). Since it is relatively nearby, at a distance of 1.3 ± 0.1 kpc (Chibueze et al. 2014; Reid et al. 2014), detailed structures that consist of four HMYSOs, MM1–MM4 (Hunter et al. 2006, 2017; Brogan et al. 2016), can be resolved with the Atacama Large Millimeter/ submillimeter Array (ALMA). Figure 1 shows the source structure traced by the ALMA 2.2 μm continuum emission (see details in Hunter et al. 2021). MM1 and MM2 are the two brightest millimeter dust sources and are associated with line-rich chemistry environments (Zernickel et al. 2012; McGuire

et al. 2017; Bøgelund et al. 2018; El-Abd et al. 2019). MM3 corresponds to a known UC HII region, NGC 6334F, which is the only source showing bright emission at mid-IR/centimeter wavelengths in the pre-outburst duration of the NGC 6334I region (de Pree et al. 1995). However, MM1 is now the brightest region at the 25, 37, and 54 μm SOFIA bands, even exceeding the UC HII region MM3 (Hunter et al. 2021). Since early 2015, a single-dish maser monitoring program conducted at the Hartebeesthoek radio observatory has detected strong flaring of many species of masers (MacLeod et al. 2018) toward NGC 6334I. Combining the millimeter outbursts detected toward MM1 (Hunter et al. 2017), it was determined that the new maser flare that occurred since 2015 is related to MM1 (Hunter et al. 2018). Further in-depth study of this source can contribute to the understanding of the physical conditions and mechanisms of accretion bursts. In this study, we present the results of a targeted line survey toward NGC 6334I, mainly for methanol and ammonia transitions that have been predicted to produce masers, using the Shanghai 65 m Tianma Radio Telescope (TMRT) from 2019 June to 2022 September. Using the new maser monitoring data and the physical conditions derived from multiple thermal methanol and ammonia lines during the accretion burst phase, these observations allow us to investigate the changes in physical conditions related to the accretion burst.

2. Observations

The survey and monitoring observations of a series of molecular lines (including masers) targeting the 6.669 GHz methanol maser source NGC 6334I (J2000 position: $17^h20^m53^s.44$, $-35°47' 02''.2$; Brogan et al. 2009) were undertaken with the TMRT from 2019 June to 2022 September. Cryogenically cooled C- ($4 \sim 8$ GHz), K- ($18 \sim 26.5$ GHz), Ka- ($26 \sim 35$ GHz), and Q-band ($35 \sim 50$ GHz) receivers and the Digital Backend System (DIBAS) were employed to receive and record signals. DIBAS is an FPGA-based spectrometer designed on the basis of the Versatile Green Bank Telescope Astronomical Spectrometer (Bussa & VEGAS Development Team 2012). Except for the C band, line survey observations were first made in the wide-band mode with a bandwidth of 1500 MHz in the K, Ka, and Q bands performed on 2019 December 15 and 19, and 2019 June 11, respectively. Because the wide-band mode has coarse spectral resolutions of $0.5 \sim 1.5$ km s^{-1} at these bands, in order to achieve higher spectral resolutions, we used the zoom-band mode to refine line profiles for the majority of the detected lines (mainly for the molecules CH_3OH and NH_3 focused on in this study) on 2020 January 9 and 13, 2019 December 22 and 2020 January 6, and 2019 June 15, for the K, Ka, and Q bands, respectively. In zoom-band mode, each narrowband window has a bandwidth of 23.4 MHz. Eight zoom-band windows can be configured to the same one sub-band to simultaneously observe spectral lines with a frequency separation of less than 1.4 GHz. For the C-band observations, we made monitoring observations with the zoom-band mode for the maser transitions, including the CH_3OH masers at 6.669 and 7.283 GHz transitions, and excited-state OH (ex-OH) masers at 6.031 and 6.035 GHz transitions. Twenty epochs were monitored for these maser transitions over a 3 yr duration from 2019 September to 2022 September. Additionally, two epochs were made on 2019 June 15 and 2022 November 12 for the 23.121, 36.169, 37.703, 38.293, 38.454, and 44.069 GHz methanol masers, and on 2020 January 9 and 2022 November 12 for the 22.235 GHz water maser, to explore the maser variability. With the active surface
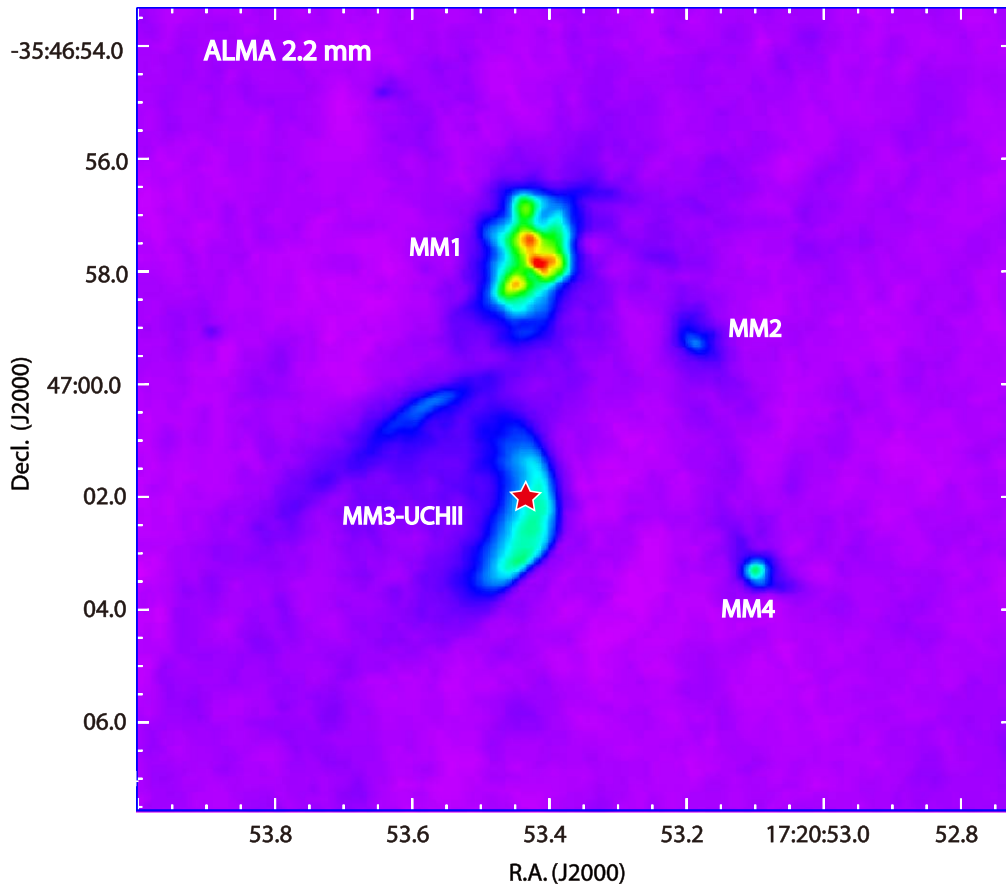
Figure 1. An overview of the source structure of the observed high-mass star-forming region NGC 6334I traced by the 2.2 mm continuum emission produced from ALMA data ADS/JAO.ALMA#2017.1.00661.S. The peak of the continuum emission is 56 mJy beam^{-1}. The pointing position of our TMRT observation is denoted with a red star.

Table 1
Paraments of the TMRT Observations

Band	Channel Number	Spectral Window (MHz)	Channel Spacing (km s^{-1})	System Temperature (K)	Sensitivity (Jy K^{-1})	Aperture Efficiency (%)	Beam Size ($''$)	Integrated Time (min)	Epoch
(1)	(2)	(3)	(4)	(5)	(6)	(7)	(8)	(9)	(10)
C	65,536	23.4	$0.014 \sim 0.017$	$20 \sim 30$	1.28	65	$147.8 \sim 187.3$	$14 \sim 24$	2019/9–2022/9
K	16,384	1500.0	$1.048 \sim 1.371$	$150 \sim 200$	1.52	55	$44.3 \sim 48.0$	$28 \sim 30$	2019/12/15
	8192	23.4	$0.033 \sim 0.047$					$24 \sim 33$	2020/1/9 and 2020/1/13
Ka	16,384	1500.0	$0.856 \sim 1.003$	$200 \sim 300$	1.59	53	$33.8 \sim 42.4$	$26 \sim 38$	2019/12/19
	4096	23.4	$0.056 \sim 0.066$					$27 \sim 38$	2019/12/22 and 2020/1/6
Q	16,384	1500.0	$0.562 \sim 0.757$	$200 \sim 300$	1.65	53	$23.8 \sim 32.0$	$18 \sim 21$	2019/6/11
	4096	23.4	$0.037 \sim 0.048$					$24 \sim 38$	2019/6/15

Note. Column (1): the C, Ku, K, Ka, and Q bands are different cryogenically cooled receivers of TMRT with frequencies in the ranges of 4−8 GHz, 12−18 GHz, 18−26.5 GHz, 30−35 GHz, and 35−50 GHz, respectively; columns (2)−(4): inherent parameters in different DIBAS modes, including channel number, bandwidth, and velocity resolution; columns (5) and (6): the system temperature and sensitivity at the corresponding observing bands; columns (7)−(8): the aperture efficiency and beam size at the corresponding observing bands; column (9): the on-source integrated time; column (10): the observation date in YY/MM/DD.

correction system, the aperture efficiency of TMRT was $53\% \sim 65\%$, and the corresponding sensitivity is $1.3 \sim 1.6$ Jy K^{-1}. The main-beam efficiency of the telescope is approximately 60% for the four-band observations.

Single-point observations were conducted in position-switching mode, as a series of repetitions of each with a 1 or 2 minute ON/OFF cycle. For each line observation, the total on-source time ranged from approximately 15–40 minutes for the C-, K-, Ka-, and Q-band observations, depending on the signal-to-noise ratio (S/N) of each detected line. A noise diode was used to perform the prior flux calibration, and the uncertainty of the flux densities for the target source was less than 10%. During the course of the observations, one or two continuum calibration sources were observed to verify the flux calibration. Additional details of the TMRT observations are presented in Table 1.

The GILDAS/CLASS package was used to perform the spectral line data reduction. The linear baseline of the spectrum was first fitted and then removed from the averaged spectrum of all scans. For weaker signals, the original high spectral resolution spectrum with a lower S/N was smoothed to 0.1–$0.3\,\mathrm{km\,s^{-1}}$ based on the line intensity, which resulted in the rms noises of the smoothed spectra ranging from 0.06–$0.10\,\mathrm{Jy}$.

3. Line Detection

In this section, we focus on the identification of the maser and thermal emissions from both the methanol and ammonia molecules detected toward NGC 6334I. From the TMRT observations, 63 CH_3OH transitions consisting of 20 maser (or maser candidate) and 43 thermal transitions, 18 $^{13}CH_3OH$ transitions, one $CH_3^{18}OH$ transition, and 34 NH_3 transitions including seven maser (or maser candidate) transitions were detected. The details of these detections are as follows. The SPLATALOGUE database, which is based on data provided by the Cologne Database for Molecular Spectroscopy (CDMS; Müller et al. 2001, 2005) and the JPL catalog database (Pickett et al. 1998), was used to identify these lines.

3.1. Methanol and Isotopic Methanol Detections

All of the detected methanol transitions are summarized in Table 2, and their line parameters are given in Table 3. Notably, We did not include the 6.669 and 7.283 GHz methanol transitions in Table 3 because they were observed in the multiepoch C-band monitoring (see Section 4.1). A number of detected transitions exhibited obvious maser characteristics. Figure 2 shows the spectra of all of the detected CH_3OH maser (or maser candidate) transitions taken with the zoom-band mode observations, with the exceptions of the 19.967 and 30.429 GHz transitions taken with the wide-band mode. We marked them in Column (6) of Table 2 as "maser" or "maser candidate." They are included in nine class II transitions and 11 class I transitions. Among them, Class II masers at 6.669, 19.967, 23.121, 37.703, 38.293, and 38.452 GHz, as well as class I masers at 36.169 and 44.069 GHz, recently have been well studied toward NGC 6334I (e.g., MacLeod et al. 2018; Hunter et al. 2018; Voronkov et al. 2014; Ellingsen et al. 2018). Additionally, for the other maser transitions shown in Figure 2, a number of narrow spectral features (spikes) with a typical line FWHM of approximately $1\,\mathrm{km\,s^{-1}}$ are overlaid on broad quasi-thermal profiles with a typical line FWHM of approximately $5\,\mathrm{km\,s^{-1}}$. Combinations of a broad profile and narrow spectral features are typically detected in maser sources. It seems reasonable to consider these transitions to harbor maser emission because their narrow spectral features (marked with arrows in Figure 2) appear at special velocities close to those of known maser transitions. In this work, we classified them as maser candidate transitions. Notably, the current single-dish observations cannot determine a high brightness temperature for the maser emission. Even for the known maser transitions with an exception for 6.7 GHz, the measured brightness temperatures are still less than 200 K (e.g., at the known 37.7 and 38.3 GHz transitions). Thus high-angular-resolution observations are required to clarify the maser nature of the candidate transitions. As a rough estimation, assuming a scale of 100 au for the maser clouds, the brightness temperature is estimated to be more than 10^4 K for the weak maser

candidate feature with a peak flux density of 0.1 Jy (see Column (10) of Table 3). Therefore, such high brightness temperature converted from the measured flux density is also coincident with the maser characteristics.

For the class II maser transitions, the majority of their emission peaks occurred at approximately $-11\,\mathrm{km\,s^{-1}}$. The 23.121, 26.121, and 28.969 GHz transitions show broad spectral emissions in the velocity range of -10 to $-2\,\mathrm{km\,s^{-1}}$, peaking at approximately $-7\,\mathrm{km\,s^{-1}}$. Combining with the spatial distributions of different maser velocity components imaged by previous interferometric observations (e.g., Ellingsen et al. 2018; Hunter et al. 2018), it can be derived that the strong class II maser components peaking at approximately $-11\,\mathrm{km\,s^{-1}}$ are mainly associated with the UC HII region MM3, but the broad emission of the three transitions and the 6.7 GHz maser component peaking at approximately $-7\,\mathrm{km\,s^{-1}}$ should be related to MM1, wherein maser flares in the multiple transitions started in early 2015 (see Hunter et al. 2018; MacLeod et al. 2018). Notably, the 7.823 GHz maser transition is peaked at a velocity of $-9\,\mathrm{km\,s^{-1}}$ according to the currently adopted frequency (see Table 2). If this transition has maser characteristics similar to others, which are peaked at $-11\,\mathrm{km\,s^{-1}}$, then its frequency should be corrected to 7823.501 MHz. Class I maser transitions generally exhibit broader line emissions in the velocity range of -12–$0\,\mathrm{km\,s^{-1}}$. Compared with previous interferometric observations, the detected class I maser spectra should be contributed by multiple positions (including MM1, MM3, and others) in the complicated region of NGC 6334I (e.g., Voronkov et al. 2014; Ellingsen et al. 2018).

The remaining 43 transitions that only show broader line profiles without significant narrow features are likely to be attributed mainly to quasi-thermal emission. We marked them as "thermal" transitions in Column (6) of Table 2. It should be noted that part of the detected transitions with broad profiles are indeed from class I $J_2 - J_1\ E$ transitions. Their methanol spectra (consisting of 16 transitions) are shown in Figure 3. The methanol spectra of other transitions (27 in total) that are not classified into the $J_2 - J_1\ E$ class I transition group are given in Figure 4. In general, our single-dish observations could not effectively distinguish whether these broader line profile transitions are maser or thermal, nor which sources are related to these emissions. Some of them did not show a particularly Gaussian profile, possibly because their spectra consisted of multiple maser components within a similar velocity range. However, to characterize the spectral characteristics of the emission, we performed a single Gaussian fitting for each of these detected transitions. For the transitions showing narrow emission, possibly from masers, we masked off the narrow emission channels from the broad profiles during fitting. The line parameters of the quasi-thermal components derived from the Gaussian fits are given Columns (4)–(7) of Table 3. Columns (8)–(9) in this table present the velocity and flux density at the peak of each maser spectral feature if the transition harbors maser emission (see above). The fitted FWHM line widths of these quasi-thermal emission are in the range of 3–$7\,\mathrm{km\,s^{-1}}$ with a mean of $5.2\,\mathrm{km\,s^{-1}}$. Comparing with velocity information of different locations from previous interferometric observations (e.g., Ellingsen et al. 2018; Hunter et al. 2018), the peaks of the quasi-thermal components are mainly at $-6 \sim -8\,\mathrm{km\,s^{-1}}$, indicating that they are likely associated with the maser flare source MM1.

Table 2
Properties of the Detected Methanol and Isotopic Methanol Transitions

Molecule	Transition	Rest Frequency (MHz)	$S\mu^2$ (D^2)	E_u/k (K)	Comment
(1)	(2)	(3)	(4)	(5)	(6)
CH_3OH	5_1-6_0A	6668.519	20.31	49.06	maser, II
	11_3-10_4E	7283.449	9.56	215.89	maser, II
	21_3-20_4E	17,910.837	26.96	583.96	thermal
	$19_6-20_5A, vt = 1$	18,220.104	33.91	907.05	thermal
	2_1-3_0E	19,967.396	3.70	28.01	maser, II
	11_1-10_2A	20,171.205	14.14	166.37	thermal
	17_6-18_5E	20,346.864	17.20	533.65	thermal
	16_4-15_5E	20,908.817	16.16	403.42	thermal
	$10_1-11_2A, vt = 1$	20,970.658	26.38	452.44	thermal
	$12_2-11_1A, vt = 1$	21,550.324	28.09	479.21	thermal
	9_2-10_1A	23,121.024	12.58	142.18	maser, II
	7_1-7_1A	23,346.879	0.85	80.09	thermal, maser, I
	10_1-9_2A	23,444.759	14.17	143.27	thermal
	27_2-27_1E	23,854.212	36.71	898.79	thermal
	3_2-3_1E	24,928.715	11.23	36.17	thermal
	4_2-4_1E	24,933.504	15.71	45.46	thermal
	2_2-2_1E	24,934.401	6.38	29.21	thermal
	5_2-5_1E	24,959.123	20.10	57.07	thermal
	6_2-6_1E	25,018.176	24.51	71.00	thermal
	7_2-7_1E	25,124.932	28.99	87.26	thermal, maser, I
	8_2-8_1E	25,294.483	33.55	105.84	thermal
	9_2-9_1E	25,541.398	38.22	126.74	thermal
	10_2-10_1E	25,878.337	42.95	149.97	thermal
	$10_1-11_2A, vt = 1$	26,120.557	26.13	452.69	thermal, maser candidate, II
	11_2-11_1E	26,313.192	47.70	175.53	thermal, maser candidate, I
	$10_9-10_8A, vt = 1$	26,550.248	11.84	811.04	thermal
	12_2-12_1E	26,847.205	52.36	203.40	thermal, maser candidate, I
	14_5-15_4E	27,283.154	14.39	367.62	thermal
	13_2-13_1E	27,472.501	56.82	233.61	thermal, maser candidate, I
	$12_2-11_1A, vt = 1$	27,700.151	28.41	479.20	thermal
	$11_9-11_8A, vt = 1$	27,817.401	15.29	836.51	thermal
	19_5-18_6E	27,820.806	19.02	576.70	thermal
	14_2-14_1E	28,169.437	60.89	266.13	thermal, maser candidate, I
	15_2-15_1E	28,905.834	64.38	300.98	thermal
	8_2-9_1A	28,969.966	12.09	121.27	thermal, maser candidate, II
	$12_9-12_8A, vt = 1$	29,113.793	17.66	864.28	thermal
	16_2-16_1E	29,636.948	67.07	338.14	thermal, maser candidate, I
	23_2-23_1E	29,972.963	55.88	662.83	thermal
	8_1-8_1A	30,010.417	0.74	98.81	thermal
	17_2-17_1E	30,308.026	68.77	377.61	thermal
	$13_9-13_8A, vt = 1$	30,429.825	19.24	894.36	thermal, maser candidate, I
	22_2-22_1E	30,752.150	60.21	609.55	thermal
	21_2-21_1E	31,209.713	63.94	558.57	thermal
	19_2-19_1E	31,226.707	68.67	463.49	thermal, maser candidate, I
	20_2-20_1E	31,358.356	66.83	509.88	thermal
	19_4-20_3E	31,977.680	25.27	536.74	thermal
	$21_5-20_6A, vt = 1$	32,379.489	37.98	954.68	thermal
	$15_9-15_8A, vt = 1$	33,088.849	20.79	961.45	thermal
	14_3-15_2E	34,236.947	18.79	306.38	thermal
	4_1-3_0E	36,169.261	10.07	28.79	thermal, maser, I
	18_4-17_5E	36,248.164	18.90	492.70	thermal
	7_2-8_1E	37,703.696	9.62	90.91	maser, II
	$6_{2,5}-5_{3,2}A$	38,293.270	3.79	86.46	maser, II
	$6_{2,4}-5_{3,3}A$	38,452.629	3.80	86.46	maser, II
	14_3-13_4A	40,405.225	15.09	293.46	thermal
	14_3-13_4A	40,635.108	15.10	293.47	thermal
	9_4-10_3E	41,110.115	7.86	192.34	thermal
	$19_3-18_2E, vt = 1$	42,284.886	50.01	762.10	thermal
	7_0-6_1A	44,069.367	24.55	64.98	thermal, maser, I
	$2_0-3_1E, vt = 1$	44,955.794	7.13	307.52	thermal
	9_3-10_2E	45,843.554	10.61	152.17	thermal
	20_7-21_6A	46,558.038	5.01	731.51	thermal

5

Table 2
(Continued)

Molecule	Transition	Rest Frequency (MHz)	$S\mu^2$ (D^2)	E_u/k (K)	Comment
(1)	(2)	(3)	(4)	(5)	(6)
	$1_0–0_0$E,vt = 1	48,247.571	3.24	302.89	thermal
	$1_0–0_0$A	48,372.460	3.23	2.32	thermal
^{13}CH$_3$OH	$2_1–3_0$E	23,980.222	0.92	27.85	thermal
	$4_2–4_1$E	27,050.524	3.92	45.01	thermal
	$5_2–5_1$E	27,071.930	5.01	56.34	thermal
	$6_2–6_1$E	27,122.720	6.11	69.94	thermal
	$7_2–7_1$E	27,215.590	7.22	85.80	thermal
	$8_2–8_1$E	27,364.077	8.35	103.93	thermal
	$9_2–9_1$E	27,581.616	9.50	124.33	thermal
	$10_2–10_1$E	27,880.030	10.68	147.00	thermal
	$12_2–12_1$E	28,747.709	13.03	199.13	thermal
	$13_2–13_1$E	29,315.200	14.15	228.61	thermal
	$14_2–14_1$E	29,955.690	15.20	260.35	thermal
	$15_2–15_1$E	30,643.720	16.13	294.35	thermal
	$16_2–16_1$E	31,342.303	16.89	330.62	thermal
	$18_2–18_1$E	32,575.520	17.70	409.92	thermal
	$12_2–11_3$E	34,711.041	3.48	199.14	thermal
	$7_0–6_1$A	35,161.580	6.13	63.41	thermal
	$8_2–9_1$A	41,904.330	3.01	119.34	thermal
	$10_1–9_2$E	44,294.420	3.14	130.11	thermal
CH$_3^{18}$OH	$10_2–10_1$E	34,831.596	40.82	144.80	thermal

Note. Columns (1)−(3): methanol or isotopic methanol molecules, transition and rest frequency referenced from the SPLATALOGUE database; columns (4) and (5): upper-level energy, and the square of the electric dipole moment for each transition; column (6): comments on the detected transitions: thermal—the transition showing a broad thermal line profile; maser (maser candidate)—the transition showing narrow maser spectral features; I or II—class I or class II methanol masers. If both thermal and maser (or maser candidate) are given, the transition contains both emissions.

In addition to the CH$_3$OH transitions, we detected 18 transitions from ^{13}CH$_3$OH and one transition from CH$_3^{18}$OH. Their spectra are shown in Figure 5, and line parameters derived from the Gaussian fits are listed in Table 3. There are no obvious narrow spectral features that were observable from these isotopic methanol spectra, suggesting nondetection of the maser. These spectra generally have a single Gaussian profile, with a typically fitted line FWHM of 4–6 km s^{-1} and peaks at velocities of $-6 \sim -8$ km s^{-1}. Therefore, they are also considered to be mainly related to the maser flare region, MM1.

3.2. Ammonia Detections

The line identification results of the NH$_3$ observations are summarized in Table 4, which includes a total of 34 transitions detected. The NH$_3$ spectra are shown in Figure 6. Table 5 summarizes the line parameters of all of the NH$_3$ transitions from Gaussian fits. All 34 NH$_3$ transitions were detected with broad profiles (with a typical line width of 4–6 km s^{-1}; see Table 5) peaking at velocities of $-6 \sim -8$ km s^{-1}. Therefore, similar to (isotopic) methanol quasi-thermal emissions, the detected NH$_3$ lines are also likely to be contributed by quasi-thermal emissions related to the maser burst region MM1.

Toward seven transitions, (1, 1), (2, 2), (3, 3), (4, 3), (6, 4), (6, 6), and (8, 6), both broad quasi-thermal and narrow feature profiles were detected. Compared with previous studies, the (3, 3), (6, 6), and (8, 6) transitions have been detected as narrow maser components (Beuther et al. 2007; Walsh et al. 2007). Therefore, in this work we identified these three transitions as "maser," and the other four transitions as "maser candidate" in Table 4. These identified possible maser features should be reliable because they are peaked at approximately

-6.6 km s^{-1} for the (1, 1), (2, 2), (3, 3), and (4, 3) transitions and at approximately 7.7 km s^{-1} for the (6, 4), (6, 6), and (8, 6) transitions. We also masked off these narrow feature channels from the broad profiles during the fitting.

Regarding transitions with hyperfine components detected at a sufficient S/N > 5, five Gaussian component fits were applied. The fitted Gaussian profiles were overlaid on the spectra shown in Figure 6. The relative intensities and velocity separations for the main and hyperfine NH$_3$ components were calculated using the SPLATALOGUE database. Using this method, we derived the optical depths of the main ammonia components in a total of 15 transitions (see Section 5.1). The optical depths are listed in Column (7) of Table 5. For the remaining transitions, it was assumed that they were optically thin.

4. Maser Variability

4.1. Maser Variability Detected from the C-band Monitoring

Two methanol maser transitions at 6.669 and 7.283 GHz and two ex-OH maser transitions at 6.031 and 6.035 GHz were monitored frequently from 2019 September to 2022 September. The maser variability of multiple velocity components from these four transitions is shown in Figure 7. The right and left circular polarization (RCP and LCP) spectral components in the two ex-OH maser transitions are illustrated separately. In Table 6, we present the statistic results for the variability behaviors of multiple velocity components from these four maser lines during our monitoring. It can be seen that majority of the maser components arrived at their maximum in 2020 July–September, except for the 6.7 GHz methanol components with velocities of > -9 km s^{-1} in 2019 September. We derived

Table 3
Line Parameters of the Quasi-thermal and Maser Components in the Detected Methanol and Isotopic Methanol

Molecule	Frequency	Date	Quasi-thermal				Maser Feature		
			V_c	T_p	δ_V	W	V_c	S_p	T_b
	(MHz)		(km s^{-1})	(K)	(km s^{-1})	(K km s^{-1})	(km s^{-1})	(Jy)	($\times 10^5$ K)
(1)	(2)	(3)	(4)	(5)	(6)	(7)	(8)	(9)	(10)
CH$_3$OH	17,910.837	2020/1/9	−6.8(0.3)	0.49(0.19)	5.49(0.79)	2.66(0.38)			
	18,220.104	2020/1/9	−7.7(0.3)	0.20(0.07)	5.73(0.80)	1.16(0.14)			
	19,967.396	2019/12/15					−10.4	70.30(0.05)	523.0
	20,171.205	2019/12/15	−5.5(0.5)	0.30(0.04)	8.75(1.11)	2.64(0.40)			
	20,346.864	2020/1/9	−6.1(0.2)	0.37(0.12)	4.79(0.49)	1.80(0.19)			
	20,908.817	2020/1/9	−6.9(0.2)	0.54(0.13)	5.15(0.41)	2.79(0.23)			
	20,970.658	2020/1/9	−6.6(0.1)	0.72(0.15)	4.70(0.32)	3.39(0.23)			
	21,550.324	2020/1/9	−5.8(0.1)	0.47(0.14)	2.39(0.38)	1.11(0.14)			
	23,121.024	2020/1/13					−11.0	11.68(0.21)	64.8
							−10.4	24.93(0.21)	138.3
	23,346.879	2020/1/13	−7.7(0.1)	0.76(0.15)	4.56(0.28)	3.48(0.21)	−9.4	0.70(0.13)	3.8
							−7.3	0.67(0.13)	3.6
	23,444.759	2020/1/13	−7.0(0.1)	1.07(0.13)	5.74(0.14)	6.12(0.14)			
	23,854.212	2020/1/13	−6.6(0.3)	0.20(0.07)	5.42(0.54)	1.07(0.11)			
	24,928.715	2020/1/13	−6.9(0.1)	1.80(0.28)	5.70(0.20)	10.26(0.39)			
	24,934.401	2020/1/13	−6.7(0.1)	2.06(0.24)	5.05(0.09)	10.40(0.16)			
	24,933.504	2020/1/13	−6.7(0.1)	1.89(0.24)	4.84(0.09)	9.13(0.16)			
	24,959.123	2020/1/13	−6.7(0.1)	1.71(0.29)	6.19(0.22)	10.58(0.43)			
	25,018.176	2020/1/13	−6.6(0.1)	2.01(0.26)	5.67(0.20)	11.40(0.44)			
	25,124.932	2020/1/13	−6.3(0.1)	1.54(0.29)	5.80(0.27)	8.94(0.49)	−8.6	1.42(0.24)	6.7
							−6.8	1.46(0.24)	6.9
	25,294.483	2020/1/13	−6.3(0.1)	2.13(0.44)	5.05(0.33)	10.78(0.63)			
	25,541.398	2020/1/13	−7.0(0.1)	1.29(0.15)	5.68(0.13)	7.31(0.16)			
	25,878.337	2020/1/13	−6.3(0.1)	1.17(0.18)	5.86(0.22)	6.86(0.25)			
	26,120.557	2020/1/13	−7.2(0.1)	2.51(0.37)	4.64(0.20)	11.62(0.54)	−10.4	1.57(0.32)	6.8
							−7.3	2.02(0.32)	8.8
							−6.6	2.36(0.32)	10.3
							−5.2	1.42(0.32)	6.2
	26,313.192	2019/12/22	−6.0(0.1)	1.21(0.16)	5.96(0.20)	7.19(0.25)	−9.9	0.47(0.14)	2.0
							−5.0	1.04(0.14)	4.5
	26,550.248	2019/12/22	−7.4(0.4)	0.25(0.09)	4.90(0.83)	1.21(0.20)			
	26,847.205	2019/12/22	−7.4(0.1)	1.38(0.16)	5.83(0.17)	8.03(0.24)	−6.8	1.10(0.13)	4.5
	27,283.154	2019/12/22	−6.9(0.1)	0.82(0.11)	4.70(0.24)	3.85(0.17)			
	27,472.501	2019/12/22	−7.6(0.1)	1.32(0.16)	5.42(0.16)	7.16(0.22)	−8.1	1.23(0.13)	4.8
	27,700.151	2019/12/22	−7.3(0.1)	0.76(0.11)	5.15(0.25)	3.93(0.18)			
	27,817.401	2019/12/22	−6.7(0.3)	0.22(0.08)	4.12(0.63)	0.91(0.14)			
	27,820.806	2019/12/19	−6.9(0.2)	0.36(0.05)	4.05(0.47)	1.44(0.18)			
	28,169.437	2019/12/22	−7.5(0.1)	0.78(0.12)	6.29(0.29)	4.91(0.25)	−9.4	0.59(0.10)	2.2
							−6.8	0.68(0.10)	2.5
							−4.5	0.43(0.10)	1.6
	28,905.834	2019/12/19	−6.7(0.1)	1.17(0.05)	5.88(0.18)	6.86(0.23)			
	28,969.966	2019/12/22	−7.8(0.2)	0.49(0.09)	6.26(0.32)	3.08(0.26)	−10.3	0.74(0.07)	2.6
	29,113.793	2019/12/19	−6.1(0.5)	0.15(0.04)	5.43(1.24)	0.82(0.17)			
	29,636.948	2019/12/22	−7.3(0.2)	0.61(0.12)	5.40(0.34)	3.30(0.21)	−8.6	0.60(0.10)	2.0
	29,972.963	2019/12/22	−7.4(0.2)	0.35(0.10)	4.74(0.48)	1.67(0.18)			
	30,010.417	2019/12/22	−8.1(0.2)	0.36(0.10)	4.78(0.52)	1.71(0.18)			
	30,308.026	2019/12/22	−7.0(0.2)	0.54(0.10)	6.45(0.32)	3.49(0.22)			
	30,429.825	2019/12/19	−7.0(0.5)	0.18(0.06)	5.37(0.90)	0.97(0.21)	−8.6	0.19(0.05)	0.6
							−5.0	0.17(0.05)	0.5
	30,752.15	2020/1/6	−7.8(0.2)	0.14(0.04)	3.52(0.46)	0.51(0.06)			
	31,209.713	2020/1/6	−8.0(0.2)	0.17(0.04)	4.99(0.48)	0.86(0.07)			
	31,226.707	2020/1/6	−7.6(0.2)	0.16(0.05)	4.50(0.44)	0.73(0.08)	−7.8	0.14(0.04)	0.4
							−4.5	0.10(0.04)	0.3
	31,358.356	2020/1/6	−7.9(0.2)	0.15(0.04)	5.37(0.50)	0.78(0.20)			
	31,977.68	2020/1/6	−7.4(0.2)	0.16(0.04)	6.77(0.60)	1.08(0.09)			
	32,379.489	2019/12/19	−6.2(0.4)	0.22(0.06)	4.52(0.78)	0.98(0.24)			
	33,088.849	2019/12/9	−7.2(0.6)	0.20(0.07)	3.99(0.92)	0.78(0.22)			
	34,236.947	2019/12/22	−6.7(0.1)	0.72(0.05)	5.99(0.24)	4.33(0.20)			
	36,169.261	2019/6/15	−8.6(0.1)	3.77(0.21)	4.12(0.04)	15.54(0.12)	−9.4	3.43(0.18)	7.8

Table 3
(Continued)

Molecule	Frequency	Date	Quasi-thermal				Maser Feature		
			V_c	T_p	δ_V	W	V_c	S_p	T_b
	(MHz)		(km s^{-1})	(K)	(km s^{-1})	(K km s^{-1})	(km s^{-1})	(Jy)	($\times 10^5$ K)
(1)	(2)	(3)	(4)	(5)	(6)	(7)	(8)	(9)	(10)
	36,248.164	2019/6/15	−6.8(0.2)	0.36(0.11)	3.61(0.45)	1.31(0.14)			
	37,703.696	2019/6/15					−11.0	42.73(0.21)	89.1
							−10.6	20.39(0.21)	42.5
	38,293.27	2019/6/15					−11.3	22.51(0.19)	45.5
							−10.8	51.44(0.19)	104.0
	38,452.629	2019/6/15					−11.3	24.27(0.21)	48.7
							−10.8	52.72(0.21)	105.7
	40,405.225	2019/6/15	−8.3(0.2)	0.50(0.16)	4.19(0.57)	2.08(0.22)			
	40,635.108	2019/6/15	−8.0(0.2)	0.59(0.17)	5.10(0.49)	2.98(0.25)			
	41,110.115	2019/6/15	−7.2(0.2)	0.73(0.20)	4.77(0.38)	3.46(0.26)			
	42,284.886	2019/6/11	−7.0(0.4)	0.45(0.13)	5.71(0.91)	2.58(0.36)			
	44,069.367	2019/6/15	−8.3(0.1)	4.33(0.67)	5.52(0.10)	23.91(0.37)	−9.4	5.18(0.58)	7.9
							−6.8	5.51(0.58)	8.4
							−3.6	2.16(0.58)	3.3
	44,955.794	2019/6/15	−7.8(0.3)	0.66(0.28)	5.19(0.55)	3.45(0.34)			
	45,843.554	2019/6/15	−7.8(0.2)	0.91(0.29)	5.89(0.56)	5.35(0.41)			
	46,558.038	2019/6/11	−6.5(0.3)	0.66(0.16)	3.87(0.61)	2.56(0.35)			
	48,247.571	2019/6/11	−7.8(0.5)	0.40(0.16)	5.54(1.21)	2.23(0.41)			
	48,372.46	2019/6/11	−8.0(0.1)	1.70(0.12)	4.83(0.22)	8.21(0.36)			
^{13}CH$_3$OH	23,980.222	2020/1/13	−7.6(0.2)	0.27(0.08)	4.08(0.38)	1.10(0.11)			
	27,050.524	2019/12/22	−6.8(0.5)	0.21(0.09)	8.00(1.18)	1.69(0.26)			
	27,071.93	2019/12/22	−7.4(0.2)	0.31(0.07)	5.84(0.49)	1.83(0.17)			
	27,122.72	2019/12/22	−7.4(0.1)	0.57(0.10)	4.52(0.26)	2.59(0.16)			
	27,215.59	2019/12/22	−7.3(0.1)	0.56(0.10)	4.73(0.33)	2.65(0.19)			
	27,364.077	2019/12/22	−7.3(0.1)	0.71(0.11)	4.87(0.26)	3.46(0.18)			
	27,581.616	2019/12/22	−7.3(0.1)	0.68(0.08)	4.28(0.22)	2.89(0.15)			
	27,880.03	2019/12/22	−7.6(0.2)	0.45(0.10)	4.65(0.45)	2.11(0.19)			
	28,747.709	2019/12/22	−7.6(0.2)	0.38(0.09)	4.80(0.42)	1.83(0.17)			
	29,315.2	2019/12/22	−6.7(0.3)	0.26(0.10)	4.92(1.01)	1.26(0.20)			
	29,955.69	2019/12/22	−7.3(0.4)	0.24(0.09)	5.54(1.03)	1.32(0.19)			
	30,643.72	2019/12/19	−6.9(0.3)	0.25(0.06)	5.34(0.92)	1.36(0.21)			
	31,342.303	2019/12/19	−6.6(0.4)	0.26(0.07)	4.83(0.79)	1.28(0.26)			
	32,575.52	2019/12/19	−7.2(0.5)	0.15(0.06)	4.08(0.84)	0.63(0.20)			
	34,711.041	2019/12/19	−8.1(0.4)	0.19(0.05)	5.45(1.13)	1.03(0.18)			
	35,161.58	2019/6/15	−6.2(0.4)	0.24(0.12)	6.80(1.31)	1.64(0.22)			
	41,904.33	2019/6/11	−6.8(0.3)	0.45(0.11)	2.96(0.67)	1.32(0.24)			
	44,294.42	2019/6/11	−6.8(0.2)	0.70(0.15)	3.30(0.64)	2.30(0.36)			
CH$_3^{18}$OH	34,831.596	2019/12/22	−8.2(0.4)	0.15(0.04)	4.27(0.84)	0.65(0.11)			

Note. Columns (1) and (2): the methanol or isotopic methanol molecules, and the transition frequency; column (3): the observation date in YY/MM/DD; columns (4)−(7): the centroid velocity, main-beam temperature of the peak, the FWHM line width and the integrated intensity of the detected quasi-thermal methanol or isotopic methanol emission; columns (8)−(9): the centroid velocity and peak flux density for the detected maser emission. column (10): the estimated brightness temperature for the detected methanol maser components at a maser cloud scale of 100 au.

the maser decay rate from the linear fit to the maser variability after their peaks, and calculated the expected ratio of the flux density at the last observational epochs in 2022 September with respect to that at the maximum. Combining previous detections, the maser variability behaviors for these four maser transitions are summarized as follows.

6.669 GHz methanol maser. The emissions from the maser components with velocities of < -9 km s^{-1} were relatively stable during our monitoring, with only approximately 10%–20% of the fluxes decreasing between the first and last epochs (see their spectra in the top-left panel of Figure 7). The maser components with velocities of > -9 km s^{-1} (particularly for −7.3, −6.6, and −5.1 km s^{-1}) show a significant decay during our monitoring, with approximately 50%–80% of the fluxes

dismissing. The methanol maser component at −7.3 km s^{-1}, which is associated with the MM1 outburst, has been reported to have started a decay since 2020 January (see Figure 3 of Hunter et al. 2021). Our detection at this velocity component was consistent with Hunter et al. (2021) for both maser flux measurements and maser variability behaviors. Combining our observations and those from Hunter et al. (2021), it can be found that this maser component decreased from the peak flux density of ∼900 Jy in 2020 January to ∼200 Jy in 2022 September, thus indicating that the maser emissions declined at a rate of 250 Jy yr^{-1}. Such a maser decay suggests that the physical conditions of the regions surrounding the MM1 have changed, for example, the radiative energy is likely decreased, resulting in a cooling process after the luminosity outburst.
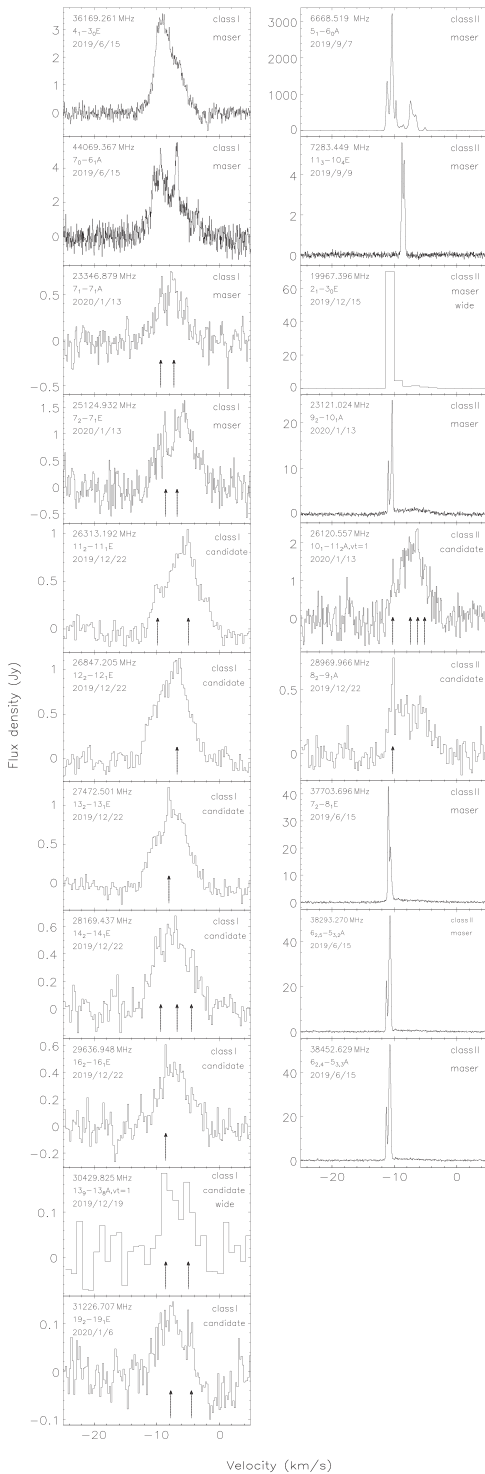
Figure 2. The left and right panels exhibit the spectra of the detected class I and II CH$_3$OH maser (or maser candidate) transitions with TMRT, respectively. The frequencies, transitions, and observing date are given in each panel. If the spectra were only taken with the TMRT wide-band mode, we marked them with "wide" in the panel. Upward arrows in the panels are indications of the possible weak and narrow maser features.

6.031 and 6.035 GHz ex-OH masers. The two maser transitions were relatively stable for the detected multiple velocity components during our monitoring. The maser components with velocities of < -9 km s^{-1} at both transitions appeared to reach their maximum in 2020 August, after which they slightly decreased by only 10%–30%. Comparing with

previous detections (during 2012–2016) reported by MacLeod et al. (2018) and Hunter et al. (2018), the maser components at velocities of < -9 km s^{-1} were nearly constant, whereas the ~ -7.8 km s^{-1} RCP and ~ -7.4 km s^{-1} LCP components underwent a significant decay with peaks of ~ 50 Jy detected in 2015 September, decreasing to only ~ 1 Jy in our monitoring. Moreover, from our monitoring, it can be found that the maser components with velocities of > -9 km s^{-1} show a more obvious decay trend than those of < -9 km s^{-1}, particularly at the 6.035 GHz transition (see Figure 7 and Table 6). Very Large Array (VLA) imaging observations revealed that the components of > -8 km s^{-1} originate from the synchrotron continuum point source CM2, whereas those of < -10 km s^{-1} were mainly from the UC HII region MM3 (Hunter et al. 2018). This may indicate that the physical conditions in the CM2 region have changed after the start of monitoring (2019 September). This change may be associated with the post-burst process from MM1, which is consistent with the 6.669 GHz methanol masers described above.

7.283 GHz methanol maser. The two velocity components from this maser transition were stable during our 3 yr monitoring observations. However, both components seemingly reached their emission maximum in 2020 July–August, similar to the ex-OH masers described above. Notably, no observations (including maser variability) have been reported for this transition toward this source in previous studies.

4.2. Other Maser Variability

4.2.1. Methanol Maser Variability

The CH$_3$OH maser transitions at 23.121, 36.169, 37.703, 38.293, 38.452, and 44.069 GHz were observed twice, on 2019 January 15 and 2022 November 12. Figure 8 shows a comparison of the spectra of the six transitions detected in the two epochs. It is clear that during a period of more than 2 yr, substantial variations in flux density and spectral profile were detected in the two class I transitions at 36.169 and 44.069 GHz, while no obvious or only small-amplitude variations in the four class II transitions at 23.121, 37.703, 38.293, and 38.452 GHz were detected.

For the four class II transitions, their flux densities and line profiles have remained stable during the past 2.5 yr. Most of the maser emissions at the four transitions were found near MM3 in the ATCA observations (Ellingsen et al. 2018). They are similar to the 6.7 GHz masers with velocities of < -9 km s^{-1}, which show a relative stable emission from the MM3 region (see above). Combining the detections at a spectral resolution of 0.2 km s^{-1} taken on 2011 March 24 with ATCA (Ellingsen et al. 2018), we found that the flux density was similar between 2011 and our two epoch observations at the 37.703 GHz transition, but a significant decrease occurred at the 38.293 and 38.454 GHz transitions. Another notable feature is that the velocities of the peaks are different for each transition observed between the ATCA and TMRT observations. Changes in flux density and peak velocity could be caused by physical or kinematic factors. For example, physical condition changes caused by the MM3 region itself, or heat-wave propagation originating from the MM1 outburst, would excite some new components and quench previous components detected with ATCA. Alternatively, the maser components may move, resulting in velocity changes along the line of sight (LOS). Notably, the velocities at the peaks also showed a small shift of
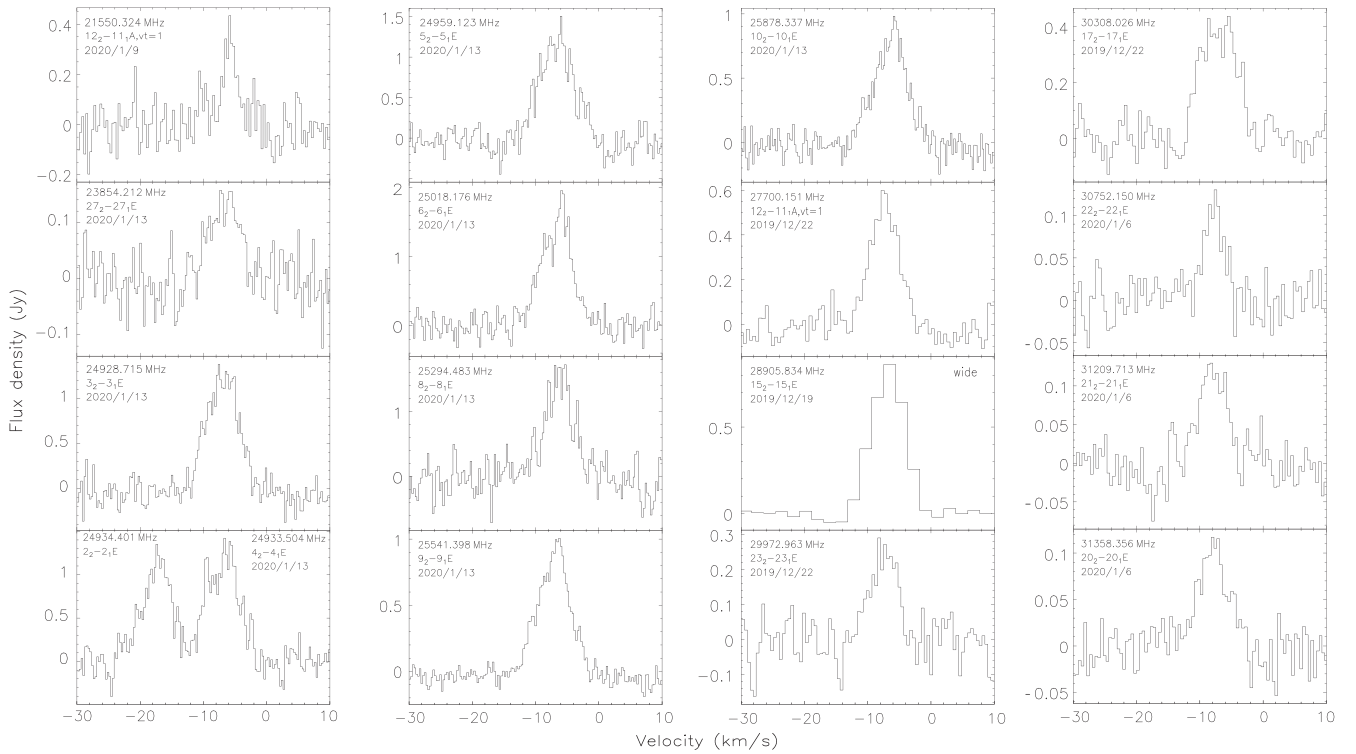
Figure 3. The TMRT spectra of the detected quasi-thermal CH$_3$OH transitions belonging to the $J_2 - J_1$ E class I group. The frequencies, transitions, and observing dates are given in each panel. If the spectra were only taken with the TMRT wide-band mode, we marked them with "wide" in the panel.

approximately 0.1 km s^{-1} during the two recent TMRT observation epochs.

For the class I transitions at 36.169 and 44.069 GHz, significant variations in the line profiles were detected between the two TMRT observation epochs. Their detections in 2019 June were mainly from blueshifted components with velocity of < -8 km s^{-1}, but in 2022 November they were mainly from redshifted components with a velocity of > -8 km s^{-1}. Both transitions increased significantly in fluxes toward the velocity components of > -8 km s^{-1}, while keeping relatively stable for the components of < -8 km s^{-1} between our observation epochs. Class I methanol maser emissions generally have wide distributions in the NGC 6334I region imaged using ATCA observations (e.g., Voronkov et al. 2014; Ellingsen et al. 2018). We only obtained the 36.2 GHz spectrum observed on 2011 March 24 with ATCA toward the same region covered by the TMRT beam, and we show it in the 36.2 GHz panel of Figure 8 for comparison. The flux density of the 36.2 GHz maser at a velocity of -9.5 km s^{-1} is only slightly increased by a factor of 0.5 between 2011 March and our two observation epochs, while the integrated emission between -2 and -8 km s^{-1} increased more remarkably, with a factor of approximately 40 between the 2011 and 2022 observations.

4.2.2. Water Maser Variability

The 22.235 GHz H$_2$O masers were also observed twice on 2020 January 9 and 2022 November 12 with TMRT. The spectra are shown in Figure 9. It can clearly be seen that significant variabilities in flux density and line profile were detected during the two epochs. The spectra had strong and narrow velocity components at -7.5 km s^{-1}, with peaks of 14,450 Jy on 2020 January 9, and 10,340 Jy on 2022 November 12; therefore, the peak component emission

decreased by a factor of $\sim$0.3 during the two epochs. The strongest emission detected at the two epochs was consistent with the long-term monitoring of H$_2$O masers reported by MacLeod et al. (2018) and Hunter et al. (2021). From the monitoring data provided by Hunter et al. (2021), we can see that the peak flux density of this component started a new decay trend from $\sim$20,000 to $\sim$15,000 Jy from 2020–2021. Combining our new data on 2022 November 12, it can be concluded that the H$_2$O masers in NGC 6334I have experienced flux decay from $\sim$20,000 to $\sim$10,000 Jy since 2020. In fact, there are a number of repeats of H$_2$O maser brightening and weakening in the range of a few thousand janskys to $\sim$15,000 Jy since its first flare in 2015 January (MacLeod et al. 2018). The H$_2$O maser spectra are complex, consisting of emissions distributed over a wide velocity range, contributed from multiple sources. The strongest maser is associated with the synchrotron continuum point source CM2 and forms a remarkable bow-shock pattern resolved with VLA observations (see details in Brogan et al. 2018). Therefore, multiple maser reflares may reflect the unstable radiation field around the bow-shock region induced by the MM1 outburst.

Another remarkable feature is that the H$_2$O maser spectral extent in the range from -75–15 km s^{-1} detected in 2020 January is wider than that of -45–0 km s^{-1} on 2022 November (see Figure 9). It means that some high-velocity masers with respect to the MM1 systemic velocity of ~ -7 km s^{-1} disappeared in the recent epoch. These high-velocity masers are likely to be associated with the highly collimated north–south bipolar outflow driven from MM1 (Brogan et al. 2018). They are possibly excited in low-mass and less-dense maser clouds, and thus have a higher motion speed compared to the other maser clouds. Their discrepancies may reflect that the
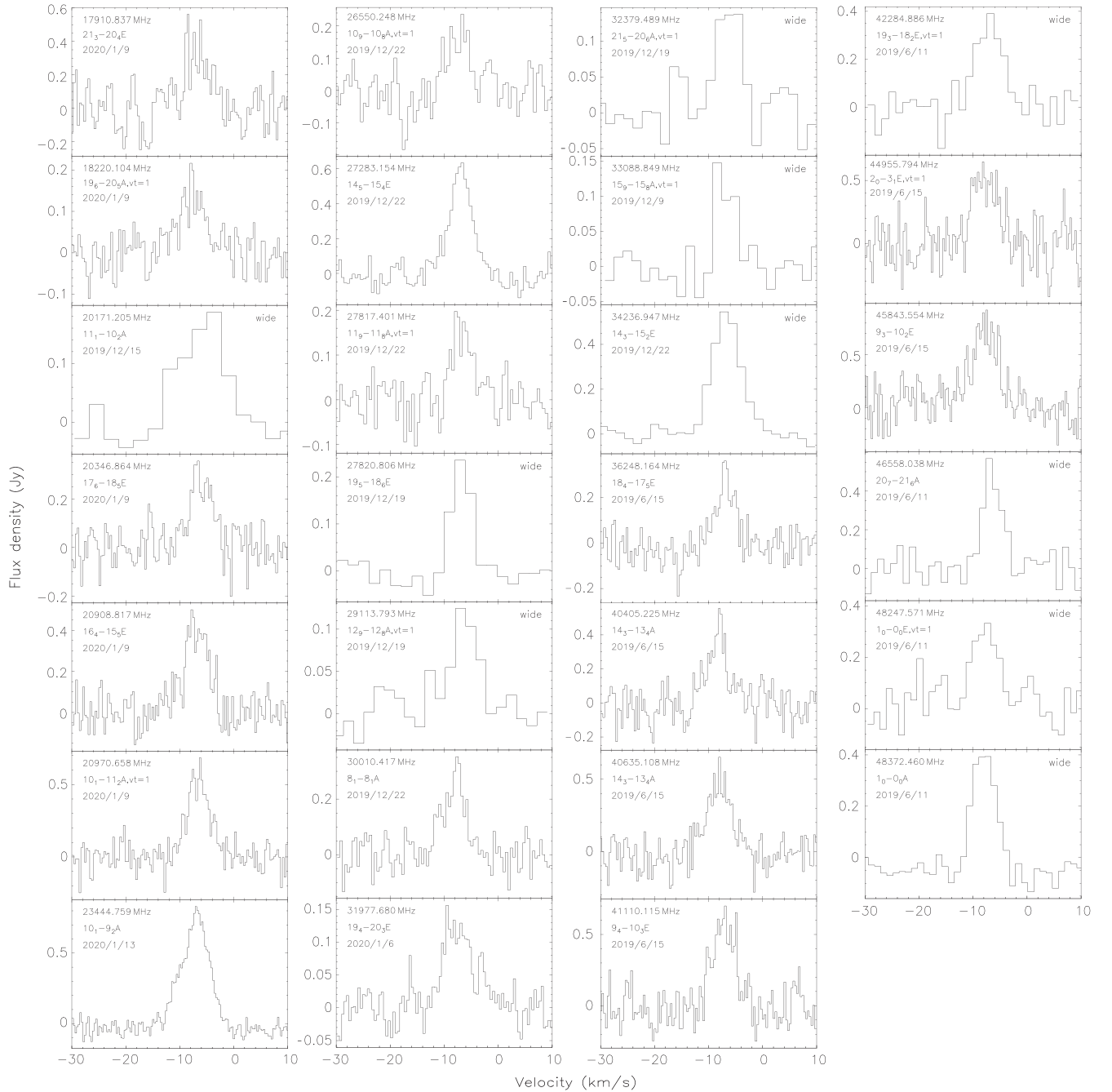
Figure 4. The TMRT spectra of the other detected quasi-thermal CH_3OH transitions that are not compiled into the $J_2 - J_1$ E class I group. The frequencies, transitions, and observing dates are given in each panel. If the spectra were only taken with the TMRT wide-band mode, we marked them with "wide" in the panel.

radiative energy of the outburst from MM1 decreases, thus reducing the pumping efficiency for masers. However, the maser emission in the velocity range from -38 to -12 km s^{-1} significantly increased in the recent observation epoch (2022 November) compared to that in 2020 June. Moreover, a new maser feature appeared at -37 km s^{-1} in the recent observation. Although the current single-dish observations cannot resolve these spectral features to accurate spatial positions, their velocity ranges are seemingly consistent with those from CM2 or MM3 UCHII-W3, or their combinations revealed with high-resolution interferometric observations (see Figure 3 of Chibueze et al. 2021).

4.2.3. Ammonia Maser Variability

Although we only observed one epoch of ammonia masers, we can still deduce some variability behaviors by comparing previous detections with Mopra and ATCA observations from 2005–2006, as reported by Beuther et al. (2007) and Walsh et al. (2007). It should be noted that the maser features detected in our observations are likely to have different velocities compared with the previous identifications of NH_3 masers. Previous observations reported one maser component at a velocity of -4.5 km s^{-1} in the (3,3) transition, and another at 5.5 km s^{-1} in the (6,6), (7,6), (8,6), (9,9), (10,9), and (11,9) transitions (Beuther et al. 2007; Walsh et al. 2007), while these
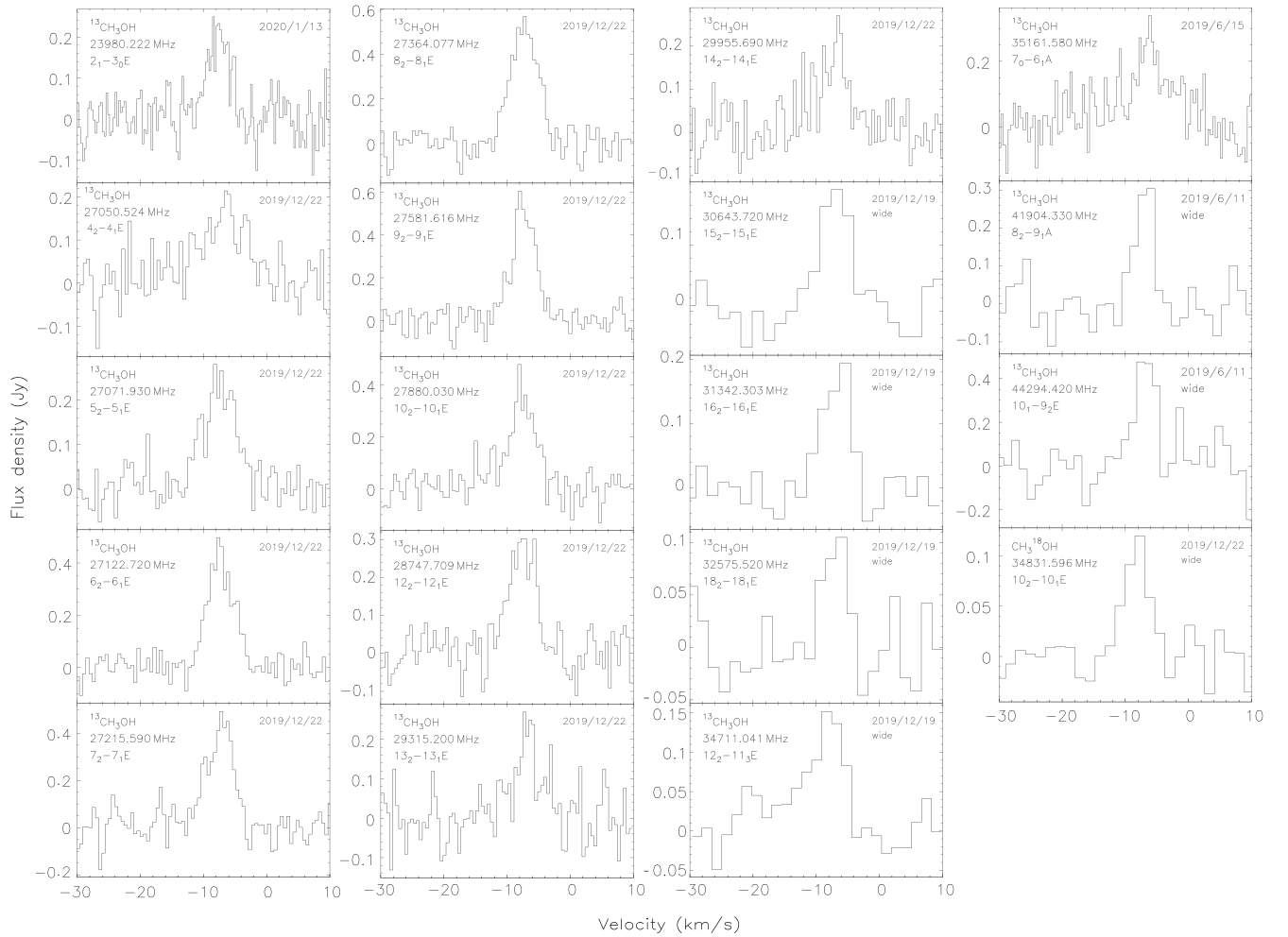
Figure 5. The TMRT spectra of the 18 ^{13}CH$_3$OH and one CH$_3^{18}$OH (at the right-lower panel) emission lines. The frequencies, transitions, and observing dates are given in each panel. If the spectra were only taken with the TMRT wide-band mode, we marked them with "wide" in the panel.

components seemingly moved to the velocity locations from -4.5 to ~ -6.2 km s^{-1} in the (6,4), (6,6), and (8,6) transitions, and from 5.5 to ~ 8 km s^{-1} in the (1,1), (2,2), (3,3), and (4,3) transitions detected in our observations. The LOS velocity differences may reflect the movement of the NH$_3$ maser components with outflow motions along the northeast–southwest direction (see Beuther et al. 2007). Alternatively, the NH$_3$ maser locations might be also changed due to the heat-wave propagation along the outflow to quench previous velocity components and excite new components. Compared to previous detections, the maser component at approximately -6.5 km s^{-1} in the (1,1), (2,2), and (4,3) transitions, as well as that at approximately 8 km s^{-1} in the (6,4) transition are newly identified in our observations. However, the maser emissions from (7,6), (9,9), (10,9), and (11,9) were not detected in our observations. These maser variabilities may be related to different physical conditions between the pre-burst and outburst stages.

4.3. Variability of Magnetic Field Strength

The magnetic field strength can be derived from the ex-OH maser velocity separation of the Zeeman pair at the RCP and LCP as ΔV km s$^{-1}/H$(mG) $= 0.079$ and 0.056 at 6.031 and 6.035 GHz, respectively (Baudry et al. 1997). To identify the Zeeman pair, we performed Gaussian fits to the ex-OH spectral

components to accurately obtain the peak value and its corresponding center velocity for both RCP and LCP. We effectively identified four Zeeman pair features for each of the 6.031 and 6.035 GHz ex-OH masers during the entire 3 yr monitoring period. The variability of the magnetic field strengths derived from these Zeeman pairs during our monitoring is shown in Figure 10. The variability of the peak flux densities of these Zeeman pairs at the RCP and LCP is also shown in this figure. The derived magnetic field strengths are in the range of 2–6 mG, all in the negative direction.

For comparison with the measurements of magnetic fields observed during 2016 October to November using VLA by Hunter et al. (2018), we matched the Zeeman pair features identified in this study to those observed with VLA. The corresponding peak flux densities of the Zeeman pairs and the derived magnetic field strengths from the VLA observations are marked with horizontal dashed lines in Figure 10 for comparison. It is clearly seen that the magnetic field strengths are nearly coincident between our single-dish and VLA observations, particularly for the (RCP and LCP) Zeeman features (-10.7 versus -10.3 km s^{-1}) and (-7.8 versus -7.3 km s^{-1}) at 6.031 GHz, and (-11.2 versus -10.9 km s^{-1}), (-10.5 versus -10.3 km s^{-1}), and (-7.7 versus -7.4 km s^{-1}) at 6.035 GHz. The magnetic field strength measured toward the Zeeman pairs (-8.7 versus -8.4 km s^{-1}) and (-8.1 versus -7.8 km s^{-1}) at

Table 4
Properties of the Detected NH_3 Transitions

Transition	Rest Frequency (MHz)	$S\mu^2$ (D^2)	E_u/k (K)	Comment
(1)	(2)	(3)	(4)	(5)
(7,3)	18,017.337	20.75	750.22	thermal
(6,1)	18,391.562	1.33	593.41	thermal
(9,6)	18,499.390	65.10	1090.89	thermal
(8,5)	18,808.507	25.30	893.33	thermal
(6,3)	19,757.538	23.89	551.31	thermal
(5,2)	20,371.450	6.29	406.92	thermal
(8,6)	20,719.221	72.49	835.46	thermal, maser
(9,7)	20,735.452	44.04	1022.61	thermal
(7,5)	20,804.830	28.60	666.03	thermal
(10,8)	20,852.527	51.89	1227.43	thermal
(6,4)	20,994.617	21.17	514.35	thermal, maser candidate
(4,1)	21,134.311	1.93	280.30	thermal
(5,3)	21,285.275	28.22	380.46	thermal
(4,2)	21,703.358	7.69	264.39	thermal
(5,4)	22,653.022	25.00	343.31	thermal
(4,3)	22,688.312	34.55	237.82	thermal, maser candidate
(6,5)	22,732.429	32.93	466.64	thermal
(3,2)	22,834.182	9.95	150.19	thermal
(7,6)	22,924.940	81.91	607.78	thermal
(2,1)	23,098.815	3.55	80.45	thermal
(8,7)	23,232.238	49.04	766.69	thermal
(9,8)	23,657.471	57.10	943.32	thermal
(1,1)	23,694.496	6.39	23.26	thermal, maser candidate
(2,2)	23,722.633	14.20	64.45	thermal, maser candidate
(3,3)	23,870.129	44.69	123.54	thermal, maser
(4,4)	24,139.416	30.60	200.52	thermal
(6,6)	25,056.025	94.33	408.06	thermal, maser
(7,7)	25,715.182	55.41	538.55	thermal
(8,8)	26,518.981	63.58	686.80	thermal
(9,9)	27,477.938	143.39	852.77	thermal
(10,10)	28,604.737	79.71	1036.40	thermal
(11,11)	29,914.486	87.61	1237.64	thermal
(12,12)	31,424.943	190.83	1456.41	thermal
(13,13)	33,156.849	103.08	1692.65	thermal

Note. Columns (1) and (2): ammonia transition and rest frequency referenced from the SPLATALOGUE database; columns (3) and (4): the upper-level energy, and the square of the electric dipole moment for each transition; column (5): comments on the observed transitions: maser—the transition showing narrow maser spectral features; thermal—the transition showing a broad thermal line profile; if both given, the transition containing both thermal and maser emissions.

6.031 GHz, and (-8.7 versus -8.5 km s^{-1}) at 6.035 GHz from our single-dish observations was slightly lower than that of VLA observations. This is likely because the single-dish observations contain additional components with velocities similar to those of the Zeeman pairs within the beam, thereby decreasing the measured magnetic field strength compared to the high-angular-resolution observations.

During our monitoring, there was no significant correlation between the variabilities of the maser flux densities and magnetic field strengths. The magnetic field strengths at the locations of the maser Zeeman pairs are likely to be stable, with some random variations within their measurement uncertainty ranges. For example, there are some Zeeman pair features at the two OH transitions showing obvious decay trends in maser flux

densities with variations larger than 40%, e.g., the pairs (-10.7 versus -10.3 km s^{-1}) at 6.031 GHz, and (-10.5 versus -10.3 km s^{-1}) and (-7.7 versus -7.4 km s^{-1}) at 6.035 GHz, while no significant trends of increment or decrement in the magnetic field strengths were found in these maser Zeeman pairs. Notably, these Zeeman pair features are mainly located in the southern parts of the UC HII region MM3 (UCHII-OH2, UCHII-OH3, and UCHII-OH4), resolved with the VLA observations (Hunter et al. 2018). Therefore, they did not trace the magnetic field circumstance associated with the luminosity outburst source MM1 or even with the southern end of the north–south outflow related to the outburst source MM1, as traced by the CS (6–5) line (see Brogan et al. 2018).

5. Rotational Diagram Analysis for the Quasi-thermal Transitions

5.1. Ammonia Transitions

It was mentioned that a number of ammonia quasi-thermal transitions showed hyperfine satellite (HFS) lines (see Figure 6). Using the main-beam temperatures T_m and T_s for the main and satellite lines derived from the five Gaussian component fits, one may calculate the optical depth τ for the ammonia transitions showing the HFS lines (Huttemeister et al. 1993):

$$\frac{T_m}{T_s} = \frac{1 - e^{-\tau}}{1 - e^{-\alpha\tau}} \quad (1)$$

$$\alpha = \frac{S\mu_s^2}{S\mu_m^2}, \quad (2)$$

where $S\mu_s^2$ and $S\mu_m^2$ are the products of the total torsion-rotational line strength and the square of the electric dipole moment of the satellite and main lines for a specific transition, respectively. All of the derived optical depth τ values for the transitions with HFS lines are summarized in Column (7) of Table 5.

In order to calculate the rotation temperature and the column density of the ammonia molecule, the local thermodynamic equilibrium (LTE) condition is assumed. The formula for the rotation diagram analysis can be derived from the following equation (e.g., Cummins et al. 1986; Chen et al. 2013; Mei et al. 2020; Zhang et al. 2022):

$$\ln\left(\frac{3kW'}{8\pi^3\nu S\mu^2}\right) = \ln\frac{N}{Q} - \frac{E_u/k}{T_{\rm rot}}, \quad (3)$$

where k is the Boltzmann constant in ergs per kelvin; W' (in units of K km s^{-1}) is the corrected line-integrated intensity of the ammonia transitions considering the optical depth τ, $W' = W\tau/(1 - \exp(-\tau))$, where W is the observed line-integrated intensity; while $W' = W$ (integrated intensity) is adopted for the optically thin transitions (i.e., those without HFS lines); ν is the frequency of the transition in hertz; $S\mu^2$ is the product of the total torsion-rotational line strength and the square of the electric dipole moment; $T_{\rm ex}$ is the excitation temperature; E_u/k is the upper-level energy in kelvin; $Q(T_{\rm rot})$ is the partition function at temperature $T_{\rm rot}$; and τ is the optical
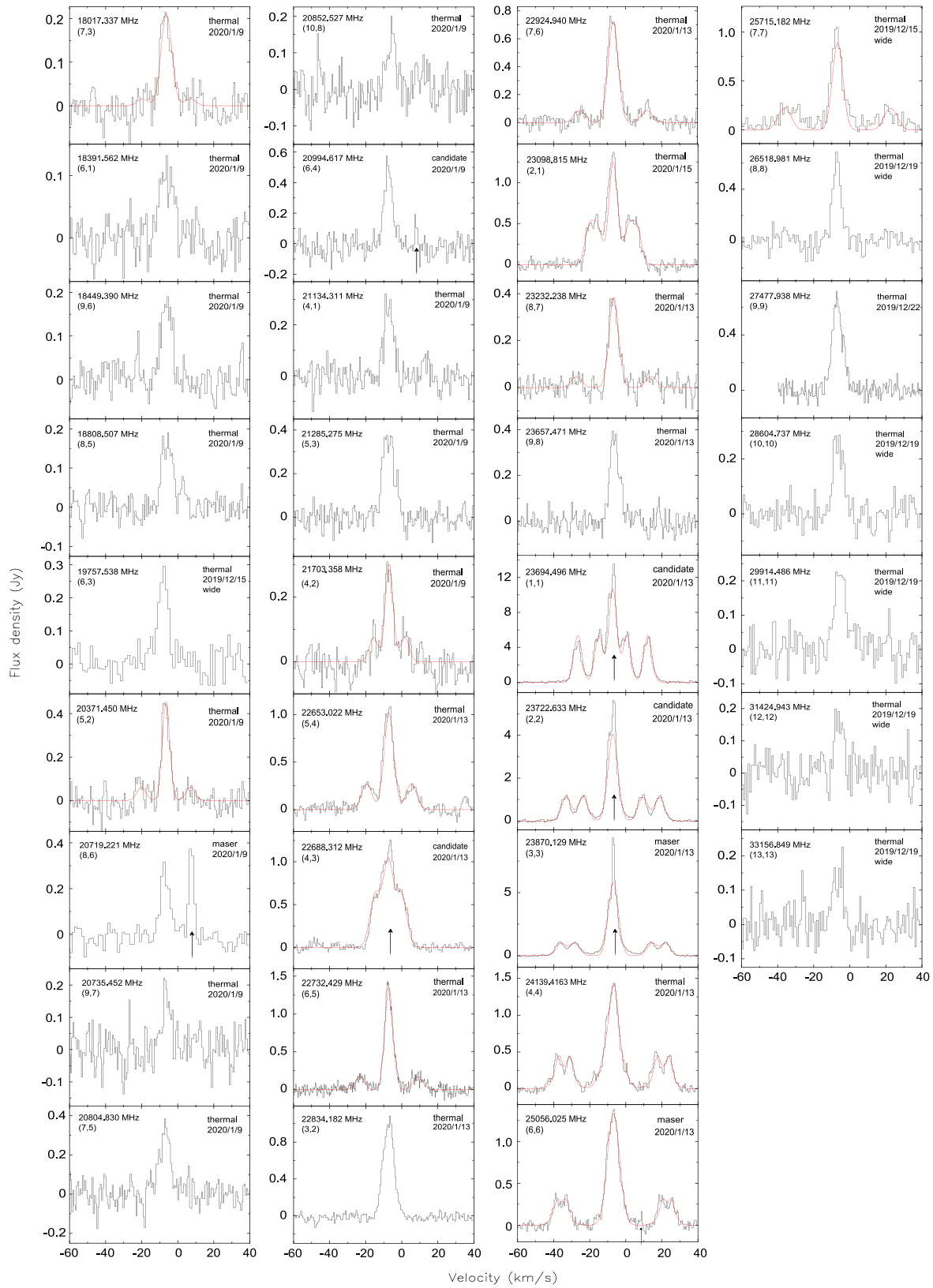
Figure 6. The TMRT spectra of the detected NH$_3$ transitions. For the transitions with hyperfine satellite lines detected, five Gaussian component fits are shown with red profiles. For the transitions with maser (or maser candidate) emission detected, their narrow features in the spectra are marked with up arrows. The frequencies, transitions, and observing dates are given in each panel. If the spectra were only taken with the TMRT wide-band mode, we marked them with "wide" in the panel.

Table 5
Line Parameters of the Quasi-thermal and Maser Components in the Detected NH_3 Spectra

Frequency	Date	Quasi-thermal					Maser Feature		
		V_c (km s^{-1})	T_p (K)	δ_V (km s^{-1})	W (K km s^{-1})	τ	V_c (km s^{-1})	S_p (Jy)	T_b ($\times 10^5$ K)
(1)	(2)	(3)	(4)	(5)	(6)	(7)	(8)	(9)	(10)
18,017.337	2020/1/9	−6.3(0.2)	0.36(0.11)	5.99(0.41)	1.89(0.11)	0.10(0.18)			
18,391.562	2020/1/9	−5.9(0.5)	0.13(0.07)	8.96(0.97)	1.21(0.12)				
18,499.390	2020/1/9	−5.9(0.3)	0.24(0.07)	6.69(0.54)	1.57(0.12)				
18,808.507	2020/1/9	−5.4(0.3)	0.23(0.08)	7.85(0.77)	1.78(0.14)				
19,757.538	2019/12/15	−7.4(0.3)	0.36(0.04)	6.40(0.76)	2.28(0.21)				
20,371.450	2020/1/9	−6.5(0.1)	0.78(0.05)	4.19(0.25)	2.85(0.15)	0.56(0.40)			
20,719.221	2020/1/9	−6.5(0.3)	0.55(0.12)	3.00(0.28)	1.76(0.21)		7.7	0.37(0.10)	2.6
20,735.452	2020/1/9	−5.9(0.3)	0.24(0.12)	5.17(0.96)	1.22(0.18)				
20,804.830	2020/1/9	−6.7(0.2)	0.42(0.12)	6.98(0.64)	2.93(0.21)				
20,852.527	2020/1/9	−5.2(0.4)	0.19(0.12)	5.68(1.15)	1.07(0.17)				
20,994.617	2020/1/9	−7.2(0.1)	0.66(0.16)	5.23(0.35)	3.43(0.19)		7.7	0.19(0.14)	1.3
21,134.311	2020/1/9	−6.9(0.2)	0.36(0.11)	5.84(0.44)	2.12(0.15)				
21,285.275	2020/1/9	−7.1(0.2)	0.48(0.10)	7.55(0.36)	3.65(0.16)				
21,703.358	2020/1/9	−7.0(0.2)	0.52(0.08)	4.32(0.27)	1.95(0.11)	0.66(0.68)			
22,653.022	2020/1/13	−7.1(0.1)	1.74(0.04)	5.36(0.11)	8.14(0.11)	9.90(1.12)			
22,688.312	2020/1/13	−7.5(0.1)	1.70(0.05)	5.63(0.16)	8.38(0.10)	0.61(0.14)	−6.2	1.28(0.06)	7.4
22,732.429	2020/1/13	−7.1(0.0)	2.30(0.02)	4.59(0.07)	9.24(0.13)	0.11(0.03)			
22,834.185	2020/1/13	−7.0(0.0)	1.32(0.11)	6.99(0.10)	9.22(0.12)				
22,924.940	2020/1/13	−6.8(0.1)	1.29(0.04)	5.52(0.12)	6.21(0.12)	0.10(0.02)			
23,098.815	2020/1/13	−7.0(0.1)	2.13(0.03)	4.82(0.09)	9.00(0.12)	0.14(0.03)			
23,232.238	2020/1/13	−6.6(0.1)	0.66(0.06)	5.26(0.22)	3.02(0.11)	0.12(0.02)			
23,657.471	2020/1/13	−6.0(0.1)	0.48(0.09)	6.01(0.29)	2.87(0.12)				
23,694.496	2020/1/13	−7.2(0.1)	18.67(0.00)	4.49(0.08)	73.39(1.22)	1.99(0.03)	−6.2	13.75(0.20)	72.6
23,722.633	2020/1/13	−7.1(0.1)	7.11(0.01)	5.52(0.13)	34.29(0.51)	4.60(0.15)	−6.2	5.93(0.08)	31.3
23,870.129	2020/1/13	−6.9(0.1)	10.15(0.00)	5.49(0.18)	48.73(1.12)	3.49(0.47)	−6.7	10.80(0.08)	56.2
24,139.416	2020/1/13	−6.6(0.1)	3.51(0.02)	4.83(0.27)	14.82(0.29)	14.59(0.34)			
25,056.025	2020/1/13	−6.4(0.3)	2.26(0.09)	6.88(0.34)	13.59(0.22)	0.30(0.04)	9.0	0.15(0.04)	0.7
25,715.182	2019/12/15	−6.7(0.2)	1.55(0.07)	5.79(0.30)	7.85(0.15)	0.11(0.02)			
26,518.981	2019/12/19	−6.7(0.2)	0.76(0.06)	4.65(0.40)	3.53(0.26)				
27,477.938	2019/12/22	−6.5(0.1)	0.87(0.10)	8.68(0.37)	7.58(0.25)				
28,604.737	2019/12/19	−5.9(0.3)	0.35(0.05)	6.66(0.57)	2.32(0.18)				
29,914.486	2019/12/19	−4.9(0.4)	0.29(0.05)	7.37(0.93)	2.15(0.21)				
31,424.943	2019/12/19	−5.6(0.2)	0.22(0.06)	4.96(0.74)	1.08(0.17)				
33,156.849	2019/12/19	−6.3(0.4)	0.19(0.05)	6.72(0.91)	1.26(0.18)				

Note. Column (1): the ammonia transition frequency; column (2): the observation date in YY/MM/DD; columns (3)–(7): the centroid velocities, main-beam temperature of peaks, the FWHM line widths, integrated intensities and optical depths of the detected quasi-thermal emissions; columns (8) and (9): the centroid velocity and flux density of peaks for the detected ammonia masers; column (10): the estimated brightness temperature for the detected ammonia maser components at a maser cloud scale of 100 au.

depth. To obtain the function of Q versus T_{rot}, a fitting was performed for the data from the SPLATALOGUE database, and the fitting result is:

$$Q \approx 0.117 T_{rot}^{1.5}. \qquad (4)$$

With the rotation diagram method, the correlation between ln $[3kW'/(8\pi^3 \nu S \mu^2)]$ and E_u/k should be linear, and the fitted straight line should have a slope of $-1/T_{rot}$ and an intercept of $\ln(N/Q)$. The rotation diagrams for the detected 34 ammonia transitions are shown in Figure 11. Notably, all 34 ammonia transitions were observed in the K and Ka bands within 1 month (from 2019 December to 2020 January; see Table 1). This avoids the effect of potentially large changes in physical condition over a long time interval in our analysis. The best fit derives an ammonia rotation temperature of 213.7 ± 20.0 K. Considering the beam dilution effect under a source scale of 7″.5, which is estimated from the combination of the ammonia

and methanol emitting regions around MM1 and MM2 (see Zernickel et al. 2012), we derived an ammonia column density of $(4.2 \pm 1.4) \times 10^{17}$ cm^{-2}.

5.2. Methanol Transitions

The analysis of the ammonia quasi-thermal transitions using the rotation diagram method can also be repeated for the CH_3OH and $^{13}CH_3OH$ ones using Equation (3). Assuming that the methanol transitions are optically thin, parameter W' in Equation (3) equals the integrated intensity W given in Table 3. Similar to the process for deriving the NH_3 partial function, we fitted the data from the SPLATALOGUE database to obtain the partial functions of CH_3OH and $^{13}CH_3OH$. The derived partial function for CH_3OH is

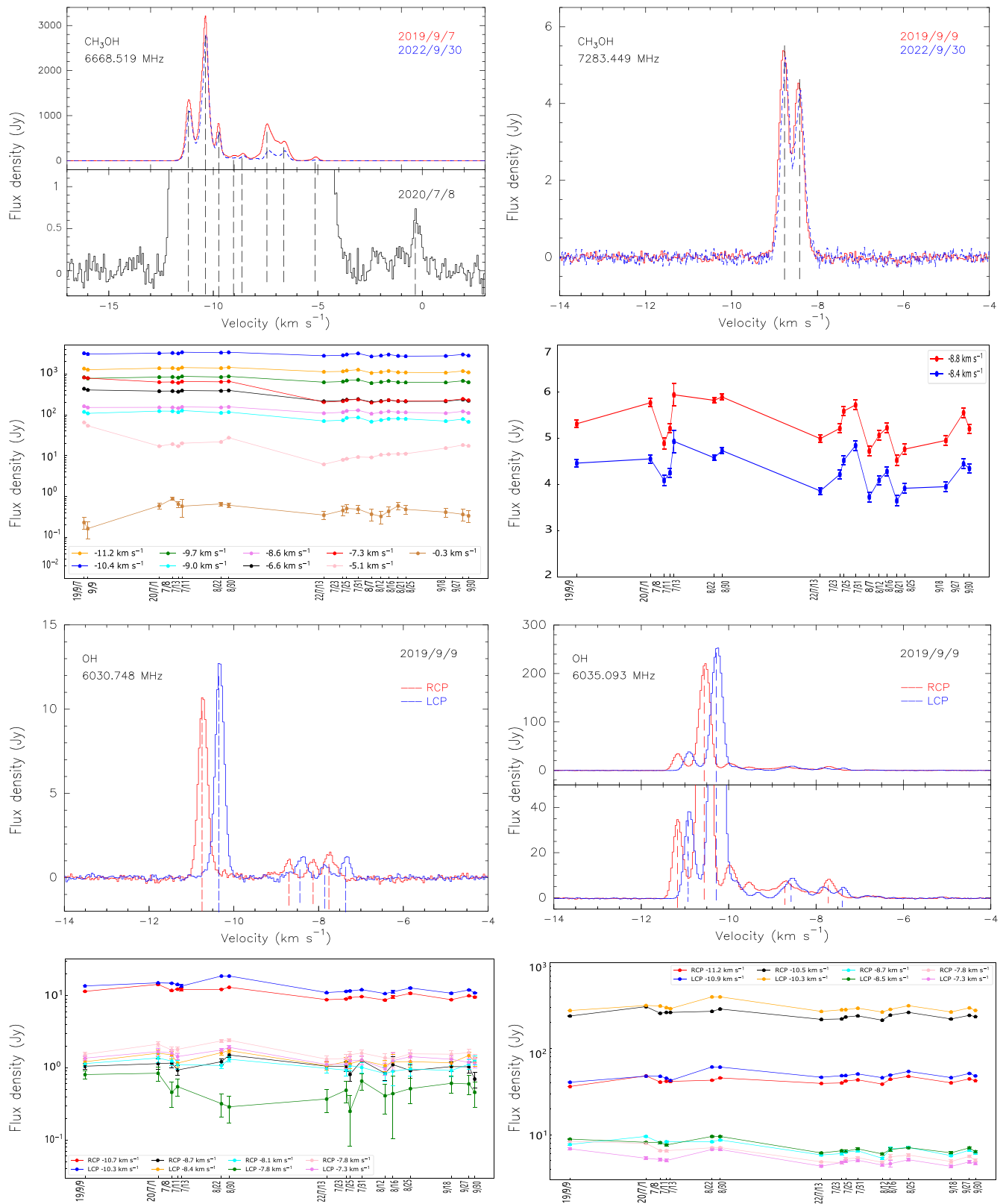$$Q \approx 1.2327 T_{rot}^{1.5}, \qquad (5)$$

Figure 7. The spectra and variabilities of different velocity components from the TMRT monitoring for the 6669 and 7283 MHz CH$_3$OH maser transitions and the 6031 and 6035 MHz ex-OH maser transitions. The peak flux densities of each velocity component (denoted with the vertical dashed line in the maser spectra shown in upper panels) at different epochs are given in the lower panel of each maser transition. For the ex-OH masers, the variabilities of the maser components taken on the RCP and LCP are given separately.

Table 6
Statistics on the *C*-band Maser Variability

Maser Transition	Component	Peak Date (km s^{-1})	Peak Flux Density (Jy)	Decay Rate (Jy yr^{-1})	Ratio
(1)	(2)	(3)	(4)	(5)	(6)
CH$_3$OH 6.669 GHz	−11.2	2020/8/30	1445	−143.8(16.1)	0.80(0.02)
⋯	−10.4	2020/8/30	3400	−250.4(38.7)	0.85(0.02)
⋯	−9.7	2020/8/30	871	−101.1(8.8)	0.77(0.02)
⋯	−9.0	2020/7/13	128	−19.9(1.8)	0.67(0.03)
⋯	−8.6	2019/9/7	162	−17.6(1.5)	0.68(0.03)
⋯	−7.3	2019/9/7	820	−201.5(5.1)	0.27(0.02)
⋯	−6.6	2019/9/7	436	−72.3(3.3)	0.51(0.02)
⋯	−5.1	2019/9/7	85	−22.6(1.1)	0.21(0.04)
CH$_3$OH 7.283 GHz	−8.8	2020/7/1	5.7	−0.4(0.1)	0.87(0.03)
⋯	−8.4	2020/7/1	4.5	−0.2(0.1)	0.89(0.04)
OH 6.031 GHz	−10.7(RCP)	2020/7/1	14.3	−1.6(0.2)	0.76(0.03)
⋯	−8.7 (RCP)	2020/8/30	1.5	−0.2(0.1)	0.74(0.08)
⋯	−8.1 (RCP)	2020/8/30	1.3	−0.1(0.1)	0.86(0.08)
⋯	−7.8 (RCP)	2020/8/30	2.4	−0.5(0.1)	0.62(0.04)
⋯	−10.3(LCP)	2020/8/30	18.6	−3.6(0.3)	0.62(0.03)
⋯	−8.4 (LCP)	2020/8/30	1.7	−0.2(0.1)	0.74(0.06)
⋯	−7.8 (LCP)	2020/7/1	0.8	⋯	⋯
⋯	−7.3 (LCP)	2020/8/30	1.9	−0.3(0.1)	0.67(0.05)
OH 6.035 GHz	−11.2 (RCP)	2020/7/1	48	−0.6(0.7)	0.97(0.03)
⋯	−10.5 (RCP)	2020/7/1	306	−19.7(4.2)	0.86(0.03)
⋯	−8.7 (RCP)	2020/7/1	9.5	−1.0(0.2)	0.78(0.04)
⋯	−7.7 (RCP)	2019/9/9	8.4	−0.9(0.1)	0.69(0.04)
⋯	−10.9 (LCP)	2020/8/30	61	−6.1(1.0)	0.80(0.03)
⋯	−10.3 (LCP)	2020/8/30	399	−57.4(6.1)	0.72(0.03)
⋯	−8.5 (LCP)	2020/8/30	9.6	−1.5(0.2)	0.69(0.03)
⋯	−7.4 (LCP)	2019/9/9	6.8	−1.0(0.1)	0.70(0.03)

Note. Column (1): maser transitions observed at the *C* band; column (2): the maser velocity component; columns (3)–(4): the epoch (YY/MM/DD) and peak flux density when the maser component arrived its maximum, respectively; column (5): the maser decay rate derived from the linear fit to maser variability after the maximum; column (6): the expected ratio of the flux density at the observational epochs in 2022 September with respect to that at the maximum.

and for ^{13}CH$_3$OH is

$$Q \approx 0.106 T_{\rm rot}^2. \qquad (6)$$

In Figure 12, the rotation diagrams for the CH$_3$OH and ^{13}CH$_3$OH transitions observed in the *K* and *Ka* bands within 1 month (see Table 1) are plotted. From this figure, it can be clearly seen that the ^{13}CH$_3$OH transitions show a good linear correlation between ln $[3kW'/(8\pi^3\nu S\mu^2)]$ and E_u/k, but the CH$_3$OH transitions have larger scatters, particularly for those with $E_u > 300$ K. These larger scatters could be caused by thermal turbulence or overheated gas from extremely hot regions, resulting in these transitions deviating from LTE conditions. Therefore, we only fitted the E-type CH$_3$OH transitions with $E_u < 300$ K (see Figure 12).

Considering the beam dilution under an emitting scale of 7″5 (similar to the ammonia analysis above), the derived column densities of CH$_3$OH and ^{13}CH$_3$OH are $(3.0 \pm 0.6) \times 10^{17}$ cm^{-2} and $(3.5 \pm 0.6) \times 10^{17}$ cm^{-2}, respectively. The rotation temperatures of CH$_3$OH and ^{13}CH$_3$OH are (84.6 ± 7.3) K and (104.9 ± 8.4) K, respectively.

6. Discussions: Special Physical Environments in NGC 6334I

6.1. High Ratio of ^{13}CH$_3$OH/CH$_3$OH

The derived ratio of ^{13}CH$_3$OH/CH$_3$OH was approximately 1 (See Section 5.2), suggesting that the ratio of ^{13}C/^{12}C is ~1 if

it follows the ratio of ^{13}CH$_3$OH/CH$_3$OH. This is obviously inconsistent with the abundance ratio of ^{12}C/^{13}C (typically 50) in the Milky Way. The high ratio of ^{13}CH$_3$OH/CH$_3$OH might be due to the following reasons.

(1) CH$_3$OH is a very abundant species in star-forming regions, suggesting that the lines of the primary 12C-isotope may be optically thick (Bøgelund et al. 2018; Lee et al. 2019). Therefore, the high ^{13}C/^{12}C ratio indicates that the column density of CH$_3$OH was underestimated owing to the high optical depth of the lines. Zernickel et al. (2012) revealed that NGC 6334I MM1 and MM2 were in regions with high methanol densities of $\sim 2 \times 10^{19}$ cm^{-2} (see below), although no methanol absorption lines were detected.

(2) McGuire et al. (2017) reported detection of interstellar methoxymethanol (CH$_3$OCH$_2$OH) toward NGC 6334I, with a column density 34 times less abundant than methanol but significantly higher than that predicted by astrochemical models. They suggested the possibility of electron-induced dissociation of CH$_3$OH. During the accretion burst, the photolysis process of methanol may be promoted because of the electron enhancement induced by UV photoionization of atomic elements originating from the increase in luminosity, which also enhances the ratio of ^{13}CH$_3$OH/CH$_3$OH.

Although item (2) may explain the abundant ^{13}CH$_3$OH detected in NGC 6334I, it still requires clarification via further quantitative chemistry models of the luminosity outburst stages. At present, item (1) is the most likely reason for the
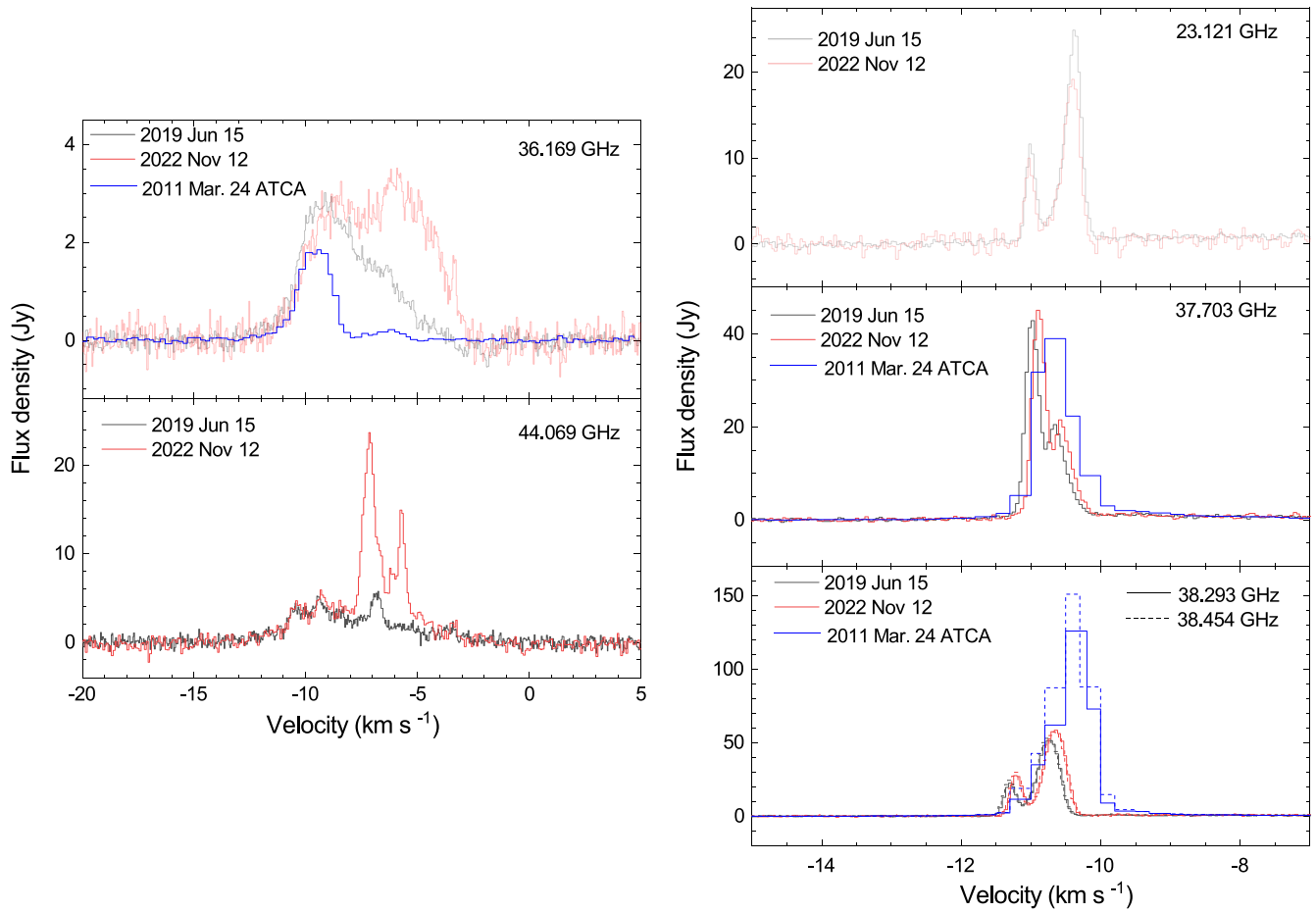
Figure 8. The left and right panels exhibit the comparisons of spectra of the class I and II CH_3OH maser transitions detected on multiple epochs with the TMRT (black and red lines) and previous ATCA observations (blue lines), respectively.
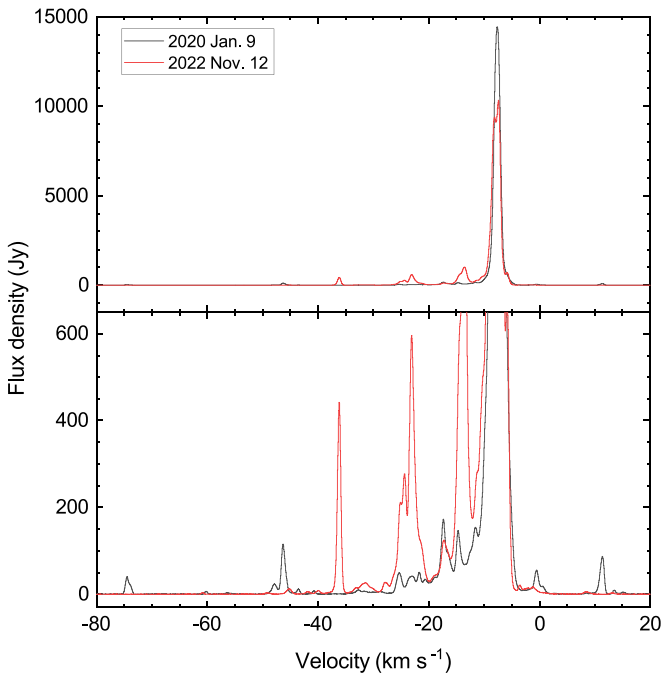

Figure 9. Comparison of the 22.235 GHz H_2O spectra taken in 2020 January and 2022 November. To clearly show the multiple velocity components with flux density of less than 650 Jy, the zoomed spectrum is presented in the lower panel.

observed high abundance of $^{13}CH_3OH/CH_3OH$ (see also Section 6.2).

6.2. Comparing with the Physical Environment of Hot Cores in the Pre-burst Stage

Zernickel et al. (2012) reported a molecular line survey toward NGC 6334I with Herschel/HIFI and the Submillimeter Array (SMA) in 2010–2011 when the MM1 was in the pre-burst stage. Abundant molecular lines ($\sim$4300) from more than 70 molecules were detected, with even detections of the high-energy levels ($E_u > 1000$ K) of the dominant emitter methanol and vibrationally excited HCN ($v_2 = 1$) from their survey. The detection of hot components mainly originated from MM1 and MM2, suggesting that the physical environment of the molecular core, wherein the MM1 is embedded, was warm even at the MM1 pre-burst stage. By comparing with two common molecules (CH_3OH and NH_3) detected in both Zernickel et al. (2012) and our surveys, we investigated the potential differences in the physical environments of hot cores between the pre-burst and outburst stages as follows:

CH_3OH. As mentioned in Section 5.2, we measured excitation temperatures of CH_3OH and its isotope in the range of 85–105 K, which is consistent with that measured for the MM1 and MM2 regions in the range of 74–104 K by Zernickel et al. (2012). Regarding column density, considering the beam dilution factor with the same scale of combining MM1 and MM2 (7$\farcs$5), the derived CH_3OH column density of 3.0×10^{17} cm^{-2} using E-type
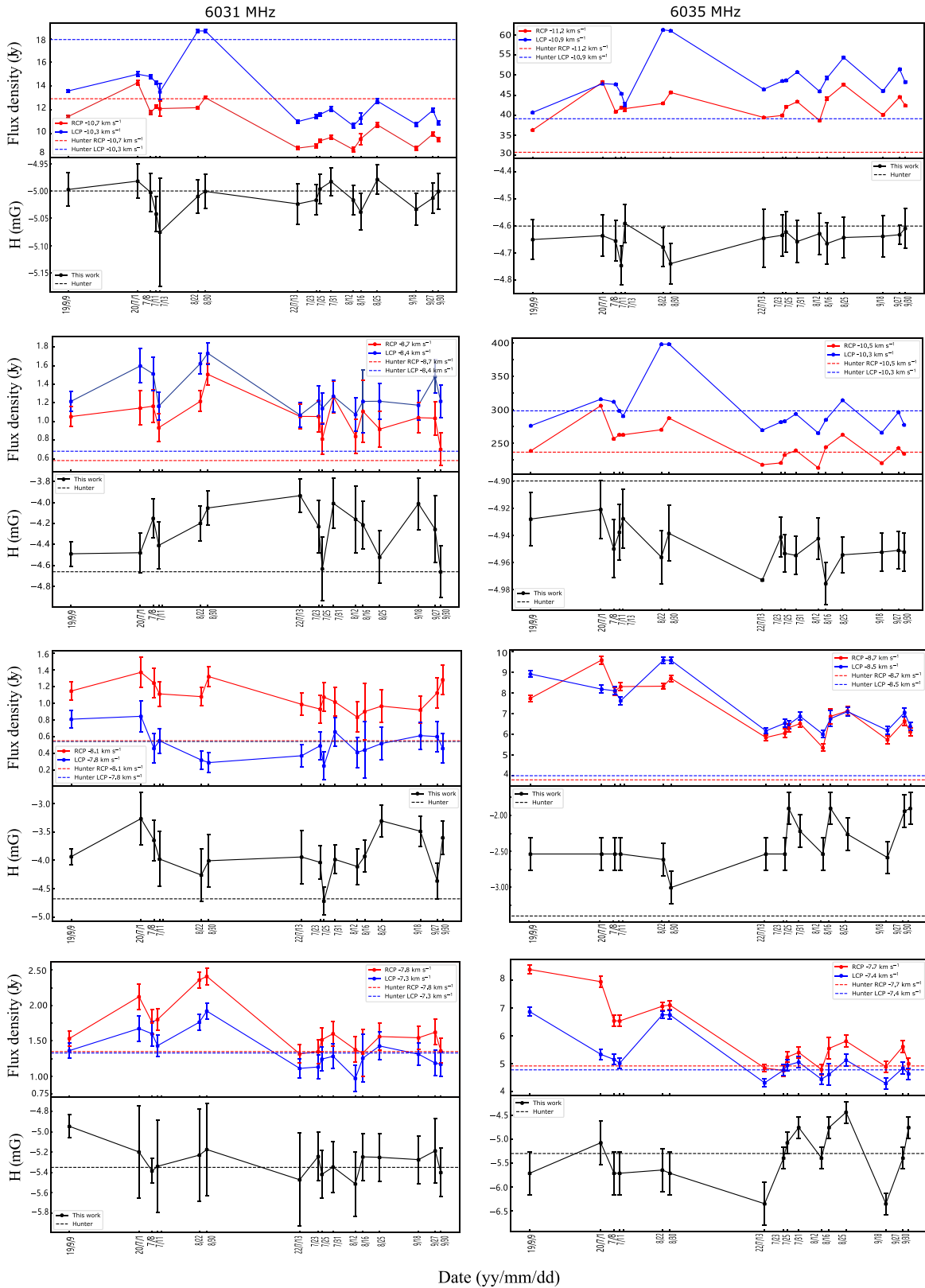
Figure 10. The variability of the magnetic field strengths from the Zeeman pairs of the detected 6.031 and 6.035 GHz ex-OH maser transitions. For each pair, the comparisons of variability between peak flux densities (upper panel) and magnetic field strengths (lower panel) are given. The corresponding flux densities and magnetic field strengths derived from Hunter et al. (2018) are given with the horizon dashed lines in each panel.

transitions with $E_u < 300$ K. This column density is 70 times lower than that of $\sim 2.0 \times 10^{19}$ cm^{-2} derived from the SMA spectra (Zernickel et al. 2012). As discussed above, the column density of CH$_3$OH may have been underestimated because the optical depths of the methanol lines were not considered in our calculations. In contrast, ^{13}CH$_3$OH is optically thin; thus, we can
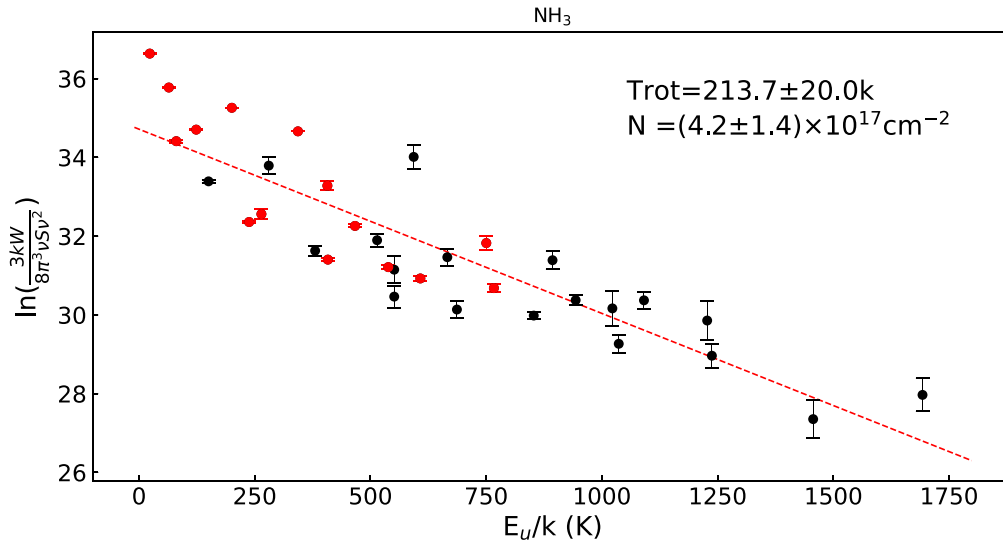
Figure 11. The rotation diagram for the detected NH_3 transitions. The red data points are for the transitions with optical depth measurements.

convert the $^{13}CH_3OH$ column density to the CH_3OH column density, which is 2.1×10^{19} cm^{-2} if $^{12}C/^{13}C = 60$ was used. This value was consistent with that reported by Zernickel et al. (2012). Therefore, in general, the methanol molecular cloud environments were coincident between the pre-burst and outburst stages of the MM1.

NH_3. Zernickel et al. (2012) derived an NH_3 cloud of a column density of 2.3×10^{16} cm^{-2} and an excitation temperature of 28 K within an emitting scale of 8″ using the Herschel/ HIFI spectra. Our observations measured a column density of $\sim 5 \times 10^{17}$ cm^{-2} and an excitation temperature of $\sim$230 K. However, it is difficult to directly compare them because there is an absence of information on whether the HIFI and our TMRT NH_3 spectra are in cospatial locations. The HIFI NH3 spectra may be more sensitive to the cold envelope gas (Zernickel et al. 2012). On the other hand, Beuther et al. (2007) measured the excitation temperatures in the range of 86–140 K using the (3,3), (4,4), (5,5), and (6,6) transitions observed with ATCA in pre-burst stage (2005 November), which is only half of our measurements. Therefore, comparison of the measured excitation temperatures between the pre-burst (by ATCA) and outburst (by TMRT) stages suggests that NH_3 gas might be heated owing to a heat wave induced by the luminosity outburst. Unlike CH_3OH, ammonia as an "interstellar thermometer" is likely more sensitive to trace the variations of gas temperatures in a burst source. Moreover, it should be noted that the broad quasi-thermal components peaking at ~ -7 km s^{-1} in the (7, 6) and (8, 6) transitions were detected in our observations, but were not in Mopra observations in 2006 November. These new detections of quasi-thermal emission are also believed to be associated with the heating process of the luminosity outburst.

6.3. Abundant Class I Methanol Transitions

A series of $J_2 - J_1$ E transitions in both methanol and isotopic methanol were detected toward NGC 6334I. These transitions are categorized to the class I transition group. Some of them showed significant narrow maser emissions (see Figure 2). Leurini et al. (2016) suggested that the class I $J_2 - J_1$ E series is the most sensitive to the density of the medium and only produces masers at higher densities than other lines.

Unlike other class I maser transitions (e.g., 36, 44, and 95 GHz), which are inverted mainly because of the predominance of $\Delta k = 0$ collisions, the $J_2 - J_1$ E series has a more complex inversion mechanism, which depends on $\Delta k \neq 0$ collisions to build up population in the $k = 1$ and 2 E-type ladders. Therefore, they are only inverted at high densities above 10^6 cm^{-3} in contrast to the other class I masers. The majority of these $J_2 - J_1$ E series showed a similar velocity range from -12 km s^{-1} to 0 km s^{-1}, which is also consistent with the 36 and 44 GHz masers (see Figure 8). This implies that the regions where these class I transitions are excited may have originated from the same or a nearby location. Our observations also included detection of the strong water maser peaking at velocity (~ -7.5 km s^{-1}) similar to those of the maser and quasi-thermal emission from the $J_2 - J_1$ E lines. As discussed in Section 4.2.2, this velocity component is associated with the luminosity outburst source MM1. Therefore, these masers are believed to be excited by physical conditions related to MM1. Because both class I methanol and water masers are pumped by the collision mechanism, the abundant masers from the $J_2 - J_1$ E, 36 and 44 GHz methanol, and strong water masers support the existence of high-density shocked regions, which may be associated with the low-velocity components of the CS (65) outflows revealed by the ALMA observations (see Figure 8 of Brogan et al. 2018). These abundant class I methanol emissions may be illuminated by the increased temperature induced by the luminosity burst source MM1. Further monitoring of class I methanol transitions (particularly for the post-burst stage) can clarify this scheme.

6.4. Comparing with Masers during the Outburst of G358.93-0.03

The known three HMYSOs with luminosity outbursts are first alerted by the 6.7 GHz methanol maser flares, e.g., NGC 6334I-MM1 (Hunter et al. 2017), S255IR-NIRS3 (Fujisawa et al. 2015), and G358.93-0.03 (Sugiyama et al. 2019). However, in HMYSOs, luminosity bursts may likely be of different kinds as in the low-mass YSO cases (FU Ori and EXor). For example, as summarized in Stecklum et al. (2021), the total accretion energy (E_{acc}) of NGC 6334I MM1 is 3.2×10^{46} erg, which is 3 times higher than that of S255IR-
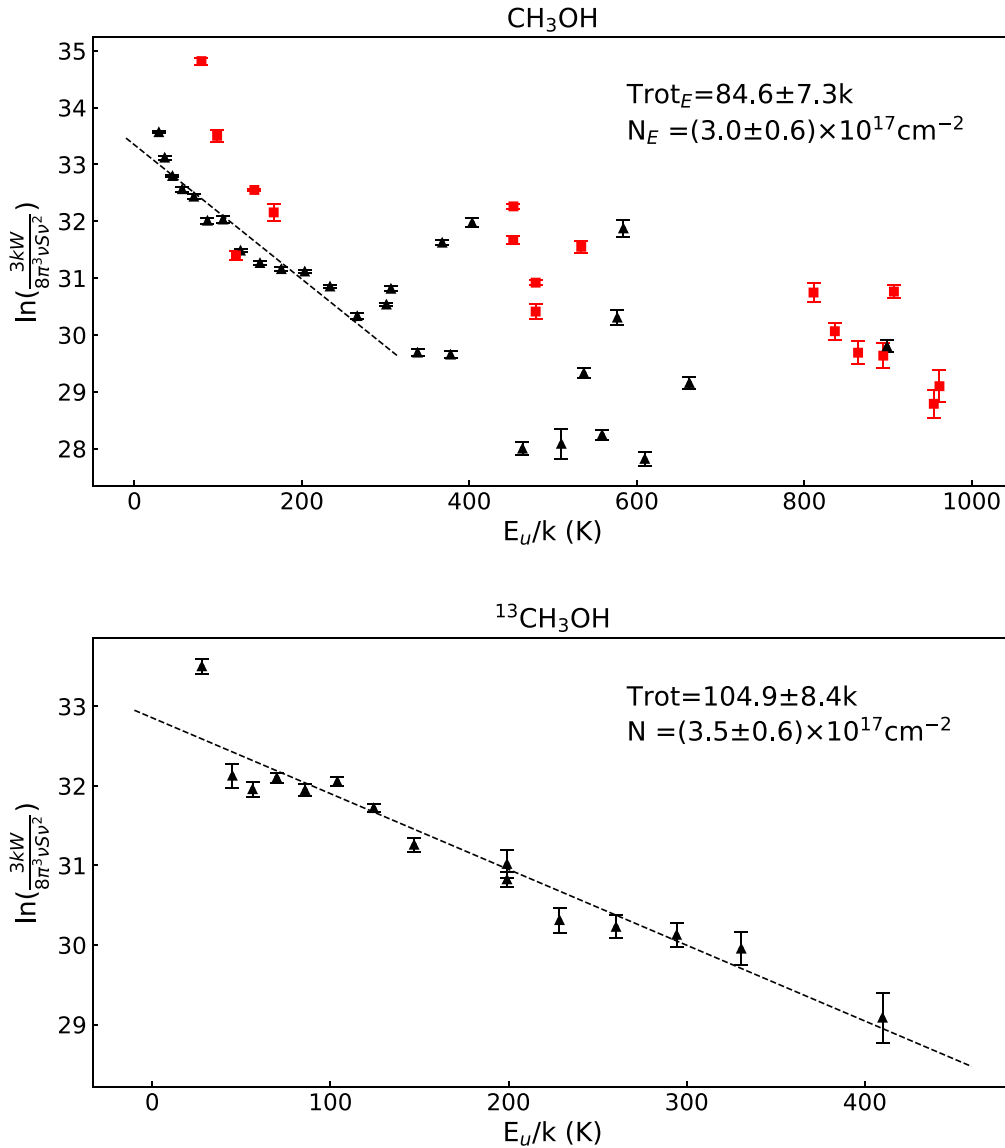
Figure 12. The upper and lower panels are rotation diagrams for the detected CH$_3$OH and ^{13}CH$_3$OH transitions at the K and Ka bands, respectively. The red data points in the upper panel are for the A-type methanol transitions. The rotation diagram fit was only made for the E-type CH$_3$OH transitions with $E_u < 300$ K in the upper panel.

NIRS3 (1.2×10^{46} erg), and 1 order of magnitude higher than that of G358.93-0.03 (2.9×10^{45} erg). Moreover, the flare event in the NGC 6334I MM1 prostar has a long duration of 40–130 yr (Hunter et al. 2021), while that in S255IR-NIR3 has a duration of a few years (Carattio Garatti et al. 2017), and G358.93-0.03 has only about half a year traced by monitoring observations of multiple methanol maser transitions (e.g., Miao et al. 2022). These distinctions imply that the magnitudes and durations of outburst events differ between the three luminosity outburst sources. Because similar surveys for NGC 633I and G358.93-0.03 were made for masers using the TMRT, we summarize the main maser properties in the two outburst sources detected with TMRT to further explore the differences of physical environments between them, as follows.

(1) The NGC 6334I MM1 maser flare areas did not exhibit class II methanol maser emissions in the past three decades. During the burst stage, the NGC 6334I MM1 6.7 GHz methanol maser reached its maximum with a peak of ∼1800 Jy and then decreased to 500–900 Jy over a period of about 2 yr,

after which it remained stable at a peak of approximately 900 Jy for a long duration of approximately 3 yr (Brogan et al. 2018; Hunter et al. 2021). Notably, since 2020, the maser showed a decay from ∼900 to ∼200 Jy over a period of ∼2.5 yr (see Section 4.1). The maser decay trend suggests that the outburst may not have the expected long duration (more than 40 yr) from Hunter et al. (2021). By contrast, the 6.7 GHz maser emission increased by 2 orders of magnitude from <10 Jy in early observations to ∼1000 Jy in 2019 mid-March (see Chen et al. 2020b and references therein), and started a rapid decay since 2019 April; thus, it has a short flare duration of half a year (e.g., Miao et al. 2022). So the 6.7 maser flare is more active in NGC 6334I MM1 than in G358.93-0.03, which is also consistent with a stronger increase in both the luminosity and accretion energy in NGC 6334I MM1 (see Hunter et al. 2021).

(2) Abundant maser emissions from the class II methanol transitions (including more than 20 transitions) were detected in the G358.93-0.03 outburst from the TMRT survey (see Miao

et al. 2022), while only 10 class II maser transitions were detected toward NGC 6334I MM1, including nine lines detected in this work and one line at 12.179 GHz (MacLeod et al. 2018). In addition to the 7.283 GHz and 28.969 GHz transitions, all eight of the other transitions detected in NGC 6334I MM1 were also observed in G358.93-0.03. Notably, the currently detected brightest components of the Class II masers originate from the UC H II region MM3 rather than from the outburst MM1 in the NGC 6334I region. These results suggest that the G358.93-0.03 outburst has a more obvious influence on the production of Class II masers. Conversely, abundant class I maser (including 11 lines) and quasi-thermal transitions (including 16 lines) were detected toward NGC 6334I from the TMRT survey and were likely associated with the MM1 outburst. Only two well-known class I transitions at 36.169 and 44.069 GHz were detectable in G358.93-0.03 (see Miao et al. 2022).

(3) Strong H_2O maser flares with more than 10,000 Jy were related to the NGC 6334I MM1 burst, but the H_2O maser flare was weak (only a few janskys) in G358.93-0.03 (Bayandina et al. 2022; Miao et al. 2022). Combining the detection of strong H_2O maser flares and rich class I transitions showing maser or quasi-thermal (both species masers produced under shock environments), it can be speculated that the NGC 6334I region has strong outflow activities to produce shocked gas in high-density environments compared to that in G358.93-0.03.

(4) Maser emissions from the new and rare molecular species were detected in the G358.93-0.03, but not in the NGC 6334I region. ^{13}C-substituted isotopic methanol ($^{13}CH_3OH$) maser, isotopic water (HDO) maser and another rare maser (HNCO) were detectable in G358.93-0.03, with a short lifetime of only ~ 1 month (Chen et al. 2020a, 2020b). Although rich lines of $^{13}CH_3OH$ were also detected in NGC 6334I, they were likely quasi-thermal rather than masers. Moreover, a low level of deuterium abundance (included in methanol deuterations) has been reported for NGC 6334I (Bøgelund et al. 2018). These results suggest that G358.93-0.03 is likely at an early evolutionary stage when its entire surrounding region has a high abundance of deuterium and a lower gas/dust temperature compared to the NGC 6334I region. Nondetection of ex-OH masers at 6.031 and 6.035 GHz in G358.93-0.03 also supports this statement.

(5) Rich ammonia emissions included in maser and thermal from multiple transitions were detected in the NGC 6334I region. In contrast, only three nonmetastable (6,3), (7,5), and (6,5) transitions were observed as maser emission toward G358.93-0.03 (McCarthy et al. 2023). However, these three transitions do not exhibit obvious maser characteristics in NGC 6334I. Our TMRT surveys toward G358.93-0.03 only detected thermal emissions at the common transitions from (1,1) to (4,4) at an rms noise level of ~ 0.1 Jy in 2019 March. These results also suggest an entire warmer environment of the molecular core due to the long-duration heating by the NGC 6334I MM1 outburst compared to G358.93-0.03.

detail. The main observational results and scientific highlights are summarized as follows.

(1) Rich transitions from (isotopic) methanol and ammonia were detected toward NGC 6334I in the TMRT survey, including 63 CH_3OH, 18$^{13}CH_3OH$, and 34 ammonia lines. Narrow maser spectral features were also identified from 20 methanol and seven ammonia transitions. These detected transitions are likely to be associated with the luminosity outburst source MM1 because they have velocities similar to those of MM1.

(2) The monitoring results of the maser variability in the C band showed a general trend that the maser components at velocities of > -9 km s^{-1} have underwent a significant decay since 2020. In particular, the 6.669 GHz methanol maser component at -7.3 km s^{-1}, which is the most closely associated with the MM1 outburst, was found to decrease from the peaks of ~ 900 Jy in 2020 January to only ~ 200 Jy in 2022 September. This maser decay suggests that the MM1 may be in the luminosity post-burst stage. Several high-velocity water masers disappeared, but some low-velocity water masers appeared between two epochs in 2020 January and 2022 November, possibly supporting the MM1 luminosity decay.

(3) Rotational diagram analysis of the ammonia and methanol transitions revealed warm regions with a high gas density surrounding MM1 and MM2. Compared with the physical environments derived from previous SMA and Herschel observations in the pre-burst stage, we found that the ammonia gas temperature was doubled (from ~ 100 to ~ 200 K), which might be associated with the molecular core being heated owing to an inside-out heat-wave propagation induced by the luminosity outburst. Some new detections of the ammonia maser and quasi-thermal emissions in our observations compared to previous observations in the pre-bust period also provide observational evidence for this statement.

(4) Comparing with the maser survey results toward another luminosity outburst source, G358.93-0.03, using TMRT, different maser species were detectable in NGC 6334I and G358.93-0.03, suggesting different physical environments associated with the two burst sources. In particular, abundant $J_2 - J_1$ E-type class I methanol masers and strong water maser flares were detected toward NGC 6334I compared to G358.93-0.03, suggesting that high-density shocked gas environments existed in NGC 6334I. However, the new and rare maser emissions from class II methanol transitions and other molecular transitions (e.g.,$^{13}CH_3OH$, HDO, and HNCO) were detectable in G358.93-0.03, but absent in NGC 6334I.

7. Summary

A systemic line survey toward the luminosity outburst source NGC 6334I MM1 was performed using the TMRT C, K, Ka, and Q bands in 2019–2020. Furthermore, multiepoch monitoring of the methanol and ex-OH masers at C-band was also taken out during 2019–2022. Both maser and thermal emissions from methanol and ammonia were explored in more

ORCID iDs

Xi Chen ● https://orcid.org/0000-0002-5435-925X
Yan-Kun Zhang ● https://orcid.org/0000-0001-7817-1975
Simon P. Ellingsen ● https://orcid.org/0000-0002-1363-5457
Shi-Ming Song ● https://orcid.org/0000-0003-3640-3875
Zhi-Qiang Shen ● https://orcid.org/0000-0003-3540-8746

References

Abraham, Z., Cohen, N. L., Opher, R., Raffaelli, J. C., & Zisk, S. H. 1981, A&A, 100, L10

Audard, M., Ábrahám, P., Dunham, M. M., et al. 2014, in Protostars and Planets VI , ed. H. Beuther et al. (Tucson, AZ: Univ. Arizona Press), 387

Baudry, A., Desmurs, J. F., Wilson, T. L., & Cohen, R. J. 1997, A&A, 325, 255

Bayandina, O. S., Brogan, C. L., Burns, R. A., et al. 2022, A&A, 664, A44

Beuther, H., Walsh, A. J., Thorwirth, S., et al. 2007, A&A, 466, 989

Bøgelund, E. G., McGuire, B. A., Ligterink, N. F. W., et al. 2018, A&A, 615, A88

Breen, S. L., Sobolev, A. M., Kaczmarek, J. F., et al. 2019, ApJL, 876, L25

Brogan, C. L., Hunter, T. R., Cyganowski, C. J., et al. 2016, ApJ, 832, 187

Brogan, C. L., Hunter, T. R., Cyganowski, C. J., et al. 2009, ApJ, 707, 1

Brogan, C. L., Hunter, T. R., Cyganowski, C. J., et al. 2018, ApJ, 866, 87

Brogan, C. L., Hunter, T. R., Towner, A. P. M., et al. 2019, ApJL, 881, L39

Burns, R. A., Sugiyama, K., Hirota, T., et al. 2020, NatAs, 4, 506

Bussa, S. & VEGAS Development Team 2012, AAS Meeting, 219, 446.10

Carattio Garatti, A., Stecklum, B., Garcia Lopez, R., et al. 2017, NatPh, 13, 276

Cesaroni, R., Moscadelli, L., Neri, R., et al. 2018, A&A, 612, A103

Chen, X., Gan, C.-G., Ellingsen, S. P., et al. 2013, ApJS, 206, 22

Chen, X., Sobolev, A. M., Breen, S. L., et al. 2020a, ApJL, 890, L22

Chen, X., Sobolev, A. M., Ren, Z.-Y., et al. 2020b, NatAs, 4, 1170

Chibueze, J. O., MacLeod, G. C., Vorster, J. M., et al. 2021, ApJ, 908, 175

Chibueze, J. O., Omodaka, T., Handa, T., et al. 2014, ApJ, 784, 114

Cummins, S. E., Linke, R. A., & Thaddeus, P. 1986, ApJS, 60, 819

de Pree, C. G., Rodriguez, L. F., Dickel, H. R., & Goss, W. M. 1995, ApJ, 447, 220

El-Abd, S. J., Brogan, C. L., Hunter, T. R., et al. 2019, ApJ, 883, 129

Ellingsen, S. P., Voronkov, M. A., Breen, S. L., Caswell, J. L., & Sobolev, A. M. 2018, MNRAS, 480, 4851

Evans, N. J. I., Dunham, M. M., Jørgensen, J. K., et al. 2009, ApJS, 181, 321

Fischer, W. J., Safron, E., & Megeath, S. T. 2019, ApJ, 872, 183

Fujisawa, K., Yonekura, Y., Sugiyama, K., et al. 2015, ATel, 8286, 1

Herbig, G. H. 1977, ApJ , 217, 693

Herbig, G. H. 1989, in ESO Workshop on Low Mass Formation and Pre-Main Sequence Objects (Garching: ESO), 233

Hirota, T., Tsuboi, M., Kurono, Y., et al. 2014, PASJ, 66, 106

Honma, M., Yoon, K. C., Bushimata, T., et al. 2004, PASJ, 56, L15

Hunter, T. R., Brogan, C. L., Megeath, S. T., et al. 2006, ApJ, 649, 888

Hunter, T. R., Brogan, C. L., MacLeod, G., et al. 2017, ApJL, 837, L29

Hunter, T. R., Brogan, C. L., MacLeod, G. C., et al. 2018, ApJ, 854, 170

Hunter, T. R., Brogan, C. L., De Buizer, J. M., et al. 2021, ApJL, 912, L17

Huttemeister, S., Wilson, T. L., Henkel, C., & Mauersberger, R. 1993, A&A, 276, 445

Kenyon, S. J., Hartmann, L. W., Strom, K. M., & Strom, S. E. 1990, AJ, 99, 869

Lee, J.-E., Lee, S., Baek, G., et al. 2019, NatAs, 3, 314

Lekht, E. E., Pashchenko, M. I., Rudnitskii, G. M., & Tolmachev, A. M. 2018, ARep, 62, 213

Leurini, S., Menten, K. M., & Walmsley, C. M. 2016, A&A, 592, A31

Liljeström, T., & Gwinn, C. R. 2000, ApJ, 534, 781

MacLeod, G. C., Smits, D. P., Goedhart, S., et al. 2018, MNRAS, 478, 1077

MacLeod, G. C., Sugiyama, K., Hunter, T. R., et al. 2019, MNRAS, 489, 3981

McCarthy, T. P., Breen, S. L., Kaczmarek, J. F., et al. 2023, MNRAS, submitted

McGuire, B. A., Shingledecker, C. N., Willis, E. R., et al. 2017, ApJL, 851, L46

Mei, Y., Chen, X., Shen, Z.-Q., & Li, B. 2020, ApJ, 898, 157

Meyer, D. M. A., Vorobyov, E. I., Elbakyan, V. G., et al. 2021, MNRAS, 500, 4448

Meyer, D. M. A., Vorobyov, E. I., Elbakyan, V. G., et al. 2019, MNRAS, 482, 5459

Meyer, D. M. A., Vorobyov, E. I., Kuiper, R., & Kley, W. 2017, MNRAS, 464, L90

Miao, D., Chen, X., Song, S.-M., et al. 2022, ApJS, 263, 9

Moscadelli, L., Sanna, A., Goddi, C., et al. 2017, A&A, 600, L8

Müller, H. S. P., Schlöder, F., Stutzki, J., & Winnewisser, G. 2005, JMoSt, 742, 215

Müller, H. S. P., Thorwirth, S., Roth, D. A., & Winnewisser, G. 2001, A&A, 370, L49

Offner, S. S. R., & McKee, C. F. 2011, ApJ, 736, 53

Omodaka, T., Maeda, T., Miyoshi, M., et al. 1999, PASJ, 51, 333

Pickett, H. M., Poynter, R. L., Cohen, E. A., et al. 1998, JQSRT, 60, 883

Reid, M. J., Menten, K. M., Brunthaler, A., et al. 2014, ApJ, 783, 130

Stecklum, B., Wolf, V., Linz, H., et al. 2021, A&A, 646, A161

Sugiyama, K., Saito, Y., Yonekura, Y., & Momose, M. 2019, ATel, 12446, 1

Volvach, A. E., Volvach, L. N., MacLeod, G., et al. 2017a, ATel, 10853, 1

Volvach, A. E., Volvach, L. N., MacLeod, G., et al. 2017b, ATel, 10728, 1

Voronkov, M. A., Caswell, J. L., Ellingsen, S. P., Green, J. A., & Breen, S. L. 2014, MNRAS, 439, 2584

Walsh, A. J., Longmore, S. N., Thorwirth, S., Urquhart, J. S., & Purcell, C. R. 2007, MNRAS, 382, L35

Zernickel, A., Schilke, P., Schmiedeke, A., et al. 2012, A&A, 546, A87

Zhang, Y.-K., Chen, X., Sobolev, A. M., et al. 2022, ApJS, 260, 34